東京大学 大学院新領域創成科学研究科
基盤科学研究系
先端エネルギー工学専攻

平成 25 年度

修士論文

Electric Field Measurement in a Channel for the Realization of a Zero-Erosion Hall Thruster

― 無損耗ホールスラスタ実現に向けた 放電室内電場計測 ―

2014 年 1 月提出
指導教員　小紫　公也　教授

47126060　伊藤　裕樹

Acknowledgement

I would like to first express the deepest appreciation to my supervisor, Prof. Kimiya Komurasaki. He gave me a great opportunity to conduct this research with the world's highest level research environment. He always guided me to an appropriate direction by giving insightful advices and suggestions.

I owe special thanks to Prof. Yoshihiro Arakawa, Prof. Hiroyuki Koizumi who gave formidable precious advices to this research. I would also like to express my gratitude for the contribution to this work made by Prof. Masakatsu Nakano, Tokyo Metropolitan College of Industrial Technology. For Mr. Bambach, who is a student of Universität Stuttgart, I cannot thank him enough for enormous contribution to this research made by him especially to the LabVIEW and Matlab coding and the development of the probes. Very special thanks also to the members of Hall thruster research group, Dr. Schönherr, Dr. Cho, Mr. Kawashima, Mr. Hosoda, Mr. Fujita, Mr. Akagi, Mr. Suzuki, and Mr. Argawal for the corroborations in experiment and fruitful discussions in seminar. I must thank my colleagues in Arakawa Komurasaki Koizumi laboratory. Finally, I would like to thank my family and friends who supported me. This research cannot be completed without them.

Table of Contents

List of Figures

List of Tables

Chapter 1

Introduction

1.1 Electric Propulsion

Electric propulsion (EP) is a technology to generate thrust by giving electric power to propellant, generally achieving higher specific impulse than that of chemical propulsion (CP) [1,2]. As a result, EP requires less amount of propellant to achieve a given thrust than CP does, which increases payload when it is applied to space mission. For space missions with large velocity increment such as deep space exploration, EP have been of great importance improving the payload ratio of spacecrafts. In addition, utilization of EP is expected to enhance the feasibility of in-space transportation of large mass structure from the viewpoint of cost, in which slight improvements in payload ratio results in reduction of great amount of propellant due to the large mass of the payload. The realization of in-space transportation of large mass structure would make space development much more active than it is with space missions such as construction of a solar power satellite or manned exploration of Mars. Therefore, researches have to be conducted to improve the performance of EP so as to enhance the feasibility of in-space transportation of large mass structure.

Another characteristic of EP is its small thrust ranging from 10 μN to 1 N, which requires EP systems to be operated for long periods to accomplish maneuvers. For example, the operational hours of an ion engine μ1 on Hayabusa, a Japanese asteroid explorer, reached 14,830 h [3]. Therefore, the lifetime is one of the most important indexes of the performance of EP. Furthermore, the lifetime is considered to be one of the essential performances to be improved for the realization of in-space transportation of large mass structure, because the accumulative operational hours of EP has to be quite long due to its large mass.

Since EP was first conceived in 1906, several concepts of electric thrusters have been developed. Those electric thrusters are generally classified into three categories in terms of the acceleration method: electrothermal, electromagnetic, and electrostatic. An arcjet thruster is classified as the electrothermal thrusters, whereas a magneto-plasma-dynamics (MPD) thruster and a pulsed plasma thruster (PPT) are electromagnetic thrusters. An ion engine and a Hall thruster are electrostatic thrusters, which have high thrust efficiency of 60 – 70%. As is shown in Figure 1.1, the specific impulse of a Hall thruster and an ion thruster is higher than that of the other electric thrusters, and it is around ten times higher than that of CP. Although the specific impulse of a Hall thruster is relatively low compared to an ion engine, the thrust density of a Hall thruster is quite higher than that of an ion engine, which shows that a Hall thruster is suitable for space missions which require large thrust.

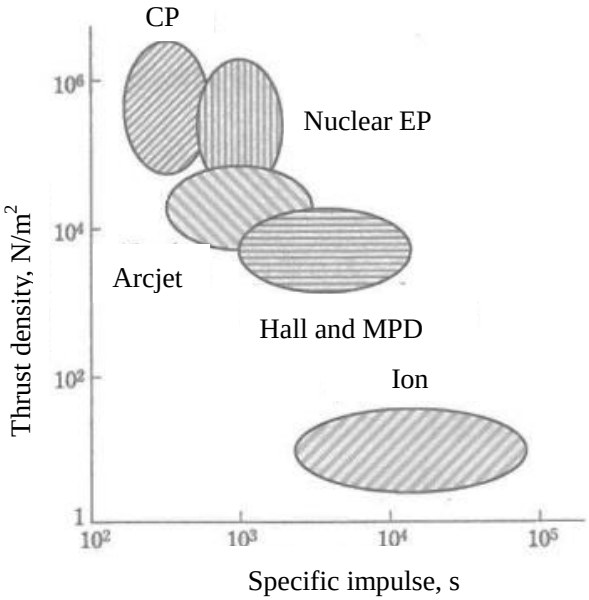

Figure 1.1 Relationship between thrust density and specific impulse of several types of thrusters [1].

1.2 Hall Thruster

A Hall thruster, as exemplarily shown in Figure 1.2, is the most actively studied electric thruster in recent years [4], which has following features.

- High thrust efficiency of higher than 50% is achieved with relatively low specific impulse of 1000 – 3000 s.
- The thrust density is higher than that of an ion engine.
- The thruster system is compact and lightweight.

Because a Hall thruster is suitable for large thrust applications, many high-power Hall thrusters were developed all over the world: SPT series thrusters (0.35 – 5 kW) developed in Russia [5], a 1.5 kW thruster PPS1350 [6] which was launched on SMART-1 [7], a lunar exploration satellite of ESA, and a 5 kW thruster at MELCO [8]. Besides, Hall thrusters with higher power up to 250 kW are actively studied in recent years [9,10,11,12,13,14].

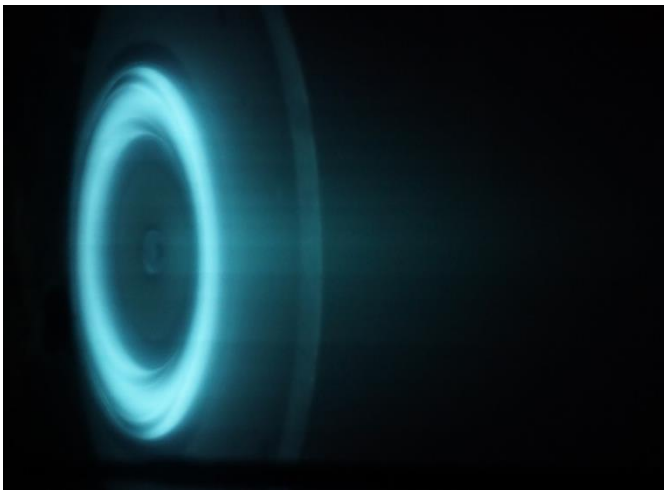

Figure 1.2 Picture of a Hall thruster UT-58 in operation.

1.2.1 Principles of Hall Thruster

The Hall thruster's principle operation is illustrated in Figure 1.3. Typically, the discharge channel has an annular shape, and radial magnetic field is imposed throughout the channel by a magnetic circuit. Because of this applied radial magnetic field, strong axial electric field is sustained throughout the discharge channel, rather than concentrated only on the near-electrode region due to the plasma Debye shielding. The electrons emitted from the cathode are trapped by the radial magnetic field due to the $\boldsymbol{E} \times \boldsymbol{B}$ drift. This azimuthal guiding center drift forms Hall current, which enables the heavy particle acceleration and thrust generation. The entrapped electrons are gradually accelerated toward the anode due to the diffusion, and ionize the propellant supplied through the anode. The ionized propellant are accelerated by the axial electric field and exhausted in high speed generating thrust. Different from ion thrusters, the ionization and ion acceleration area is not separated in Hall thrusters, and the quasi-neutrality is sustained throughout the discharge channel with the exception of sheath region. This feature enables Hall thrusters to achieve much higher thrust density than ion thrusters, because the current density is not limited by the Child-Langmuir law. The cathode has the function of not only an electron source but also a neutralizer that the entire system is electrically neutralized by emitting excess electrons. It is to be noted that the exhausted propellant ion beam itself is not necessarily neutralized. In summary, the thrust of Hall thrusters is generated by the electric static acceleration of propellant, whereas the thrust is transferred to the thruster by electromagnetic force generated by the Hall current. This is why the Hall thrusters are classified to the electrostatic thrusters, though they have the features of electromagnetic thrusters at the same time.

There are three fundamental design criteria of Hall thrusters as written follows:

$$\omega_e \tau_e \gg 1. \tag{1.1}$$

$$r_e \ll l \ll r_i. \tag{1.2}$$

$$\lambda_n \ll l \ll \lambda_i. \tag{1.3}$$

Where, ω_e is electron cyclotron frequency, τ_e is electron's characteristic time of collision, $\omega_e \tau_e = \Omega_e$ is electron Hall parameter, l is characteristic length of discharge channel, r_e and r_i are respectively Lamor radius of electron and ion, and λ_n and λ_i are collision mean free path of neutral and ion, respectively. First, Eq. (1.1) means the cyclotron frequency should be much higher than the collision frequency for electrons that the electrons should be well confined by the applied magnetic field. Second, Eq. (1.2) indicates that only the electrons are trapped by the magnetic field but the ions are exhausted without suffering guiding center drift. Finally, Eq. (1.3) denoted that the neutral propellants should be efficiently ionized within the discharge channel, whereas the ions should be exhausted before they recombine with electrons. Generally, these three fundamental criteria are easily satisfied and more detailed considerations are necessary for actual Hall thruster design.

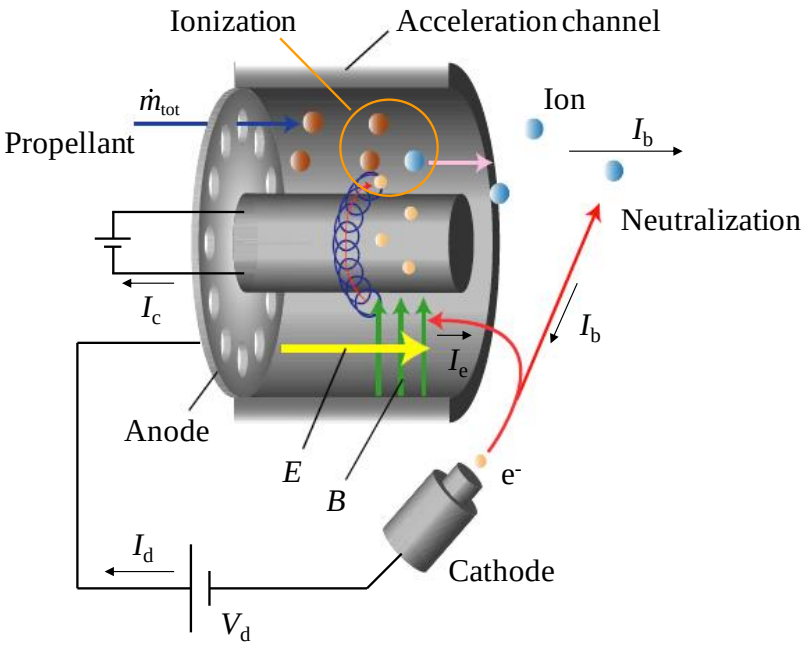

Figure 1.3 Principle of Hall thruster operation.

1.2.2 Types of Hall Thruster

Hall thrusters are usually classified to two major types according to their acceleration mechanism as follows:

- Stationary Plasma Thruster (SPT)
- Thruster with Anode Layer (TAL)

SPTs were first developed by Morozov during 1960s [5], whereas TALs were first developed by Zharinov [15]. The schematics of both thrusters are shown in Figure 1.4.

SPTs have a dielectric ceramic discharge channel wall, usually Boron Nitride (BN). The major advantage of SPTs is that their operation is very stable and has small discharge oscillation amplitude. Consequently, SPTs are the most developed and the most used Hall thrusters for satellite missions. On the other hand, the electron wall loss is relatively high because of the secondary electron emission from the wall, which is the main energy loss mechanism of SPTs. Thus, usually SPTs have relatively long channel length for sufficient propellant ionization, because the electron temperature is regulated to low level. This is the major disadvantage of SPTs that the plasma inflow to the wall is intense which decreases the thrust performance.

In comparison, TALs have a metallic channel wall biased to cathode potential to minimize the electron wall loss. Thus, the electron temperature inside the TALs is usually higher than that of the SPTs, and the necessary channel length is accordingly shorter. There exists near anode electron sheath in TALs and the propellant acceleration inside this anode layer is significant, which is the reason why the TALs is called anode layer type. Compared with SPTs, TALs have the disadvantages of larger discharge oscillation and lower operation stability, which results in the limited use of TALs for flight missions. However, TALs have advantages in the thrust performance, which is typically higher than that of SPTs due to the reduced plasma wall loss. Therefore, this research focuses on TALs.

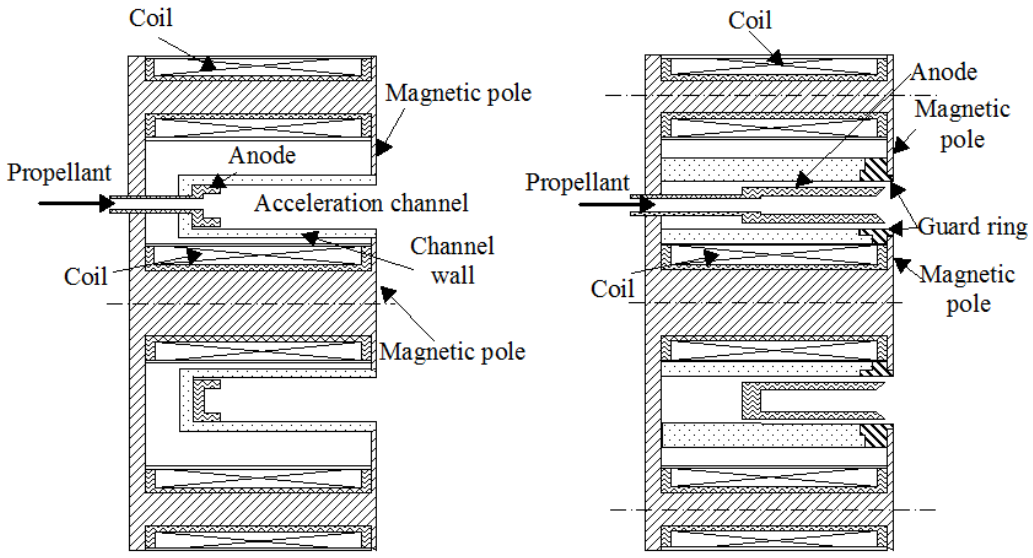

Figure 1.4 Schematics cross section of magnetic layer type (left) and anode layer type (right) Hall thrusters.

1.3 Solar Power Satellite

A Hall thruster is considered to have less difficulty to develop high power thrusters which are necessary for in-space transportation of large mass structure. A solar power satellite (SPS) is one of satellites which require such in-space transportation. The concept of a SPS is to generate power in orbit and transmit the power to Earth [16]. SPSs have several advantages: 1) SPSs utilize renewable energy, 2) photovoltaic cells yield 5 - 10 times higher power in orbit compared to the ones on Earth [17], 3) power generation of SPS is stable. Among these advantages, the stability of power generation is most important, as the abrupt fluctuation of power generation is a continuing issue in the utilization of renewable energy [17]. However, the typical mass of a SPS is in the range of tens of thousands of tons making it difficult to construct a SPS system using current transportation means from the view point of the transportation cost. Therefore, this research first focuses on the cost analysis of in-space transportation of a SPS using Hall thruster propulsion systems to deduce the specifications that Hall thrusters for in-space transportation should have.

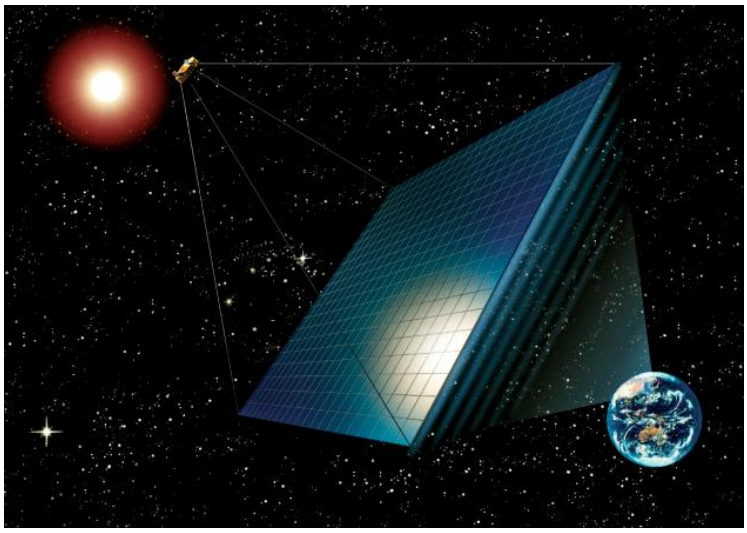

Figure 1.5 SPS planned by USEF [17].

1.4 Lifetime of Hall Thruster

It is expected that the lifetime is one of most important performances of Hall thruster for in-space transportation of large mass structure, because Hall thruster has to be operated for long period due to its small thrust and to the large mass of the payload. The most serious limitation of the lifetime of a Hall thruster is the channel wall erosion caused by ion sputtering. Ion sputtering is a process whereby atoms or molecules are ejected from a solid material surface with the incidence of high energetic ions. For the channel wall erosion of a Hall thruster, ions accelerated toward the channel wall due to the electric field formed near the wall causes the erosion.

Since a Hall thruster is expected to be operated for long period, many researches have been conducted to evaluate the lifetime of the thruster by measuring the magnitude of erosion. For example, the endurance tests of the thrusters using ground facilities are frequently conducted [8,18,19,20,21], as well as the development of instantaneous measurement method of the wall erosion [22,23]. In addition, to develop a Hall thruster with less wall erosion, the models of ion sputtering were examined based on experimental and computational results [24,25,26]. In consequence, it was reported that BPT-4000 (a 4.5 kW SPT) reached a zero-erosion configuration judging from the measurement of wall erosion through its duration test conducted in 2010 [20]. The mechanism of this was examined based on numerical simulations with the conclusion that a certain configuration of magnetic field would work as a shielding of the walls [27], which was supported by experimental results [28]. This technology was named as magnetic shielding.

The principle of the magnetic shielding for SPTs is illustrated in Figure 1.6. The magnetic field lines of the unshielded thrusters cross the channel walls (Figure 1.6 (b)), whereas the magnetic field lines of the magnetically shielded thrusters is parallel to the channel walls (Figure 1.6 (c)) [28], which can be realized by modifying the geometric configuration and the magnetic field configuration of the channel. Because the equipotential lines forms along the magnetic field lines if the electron temperature along the magnetic field lines is low [29], the parallel magnetic field lines near the walls causes electric field which repels the ions from the channel walls resulting in the reduction of the channel wall erosion, as shown in Figure 1.7.

The magnetic shielding is applied only to SPTs so far, and it has never been applied to TALs, although the thrust efficiency of which is generally higher than that of SPTs. However, because the electrical potential of the channel walls of TALs is different from that of SPTs, the electric field near the channel walls is not clear in the case of TALs. Therefore, to realize the longer lifetime Hall thrusters with high thrust efficiency, the geometric configuration of the magnetic shielding, the application of which would not change the thrust performance greatly, was applied to TALs and the electric field and electron temperature inside the discharge chamber of a TAL was measured to obtain a criteria for zero-erosion TALs in this research.

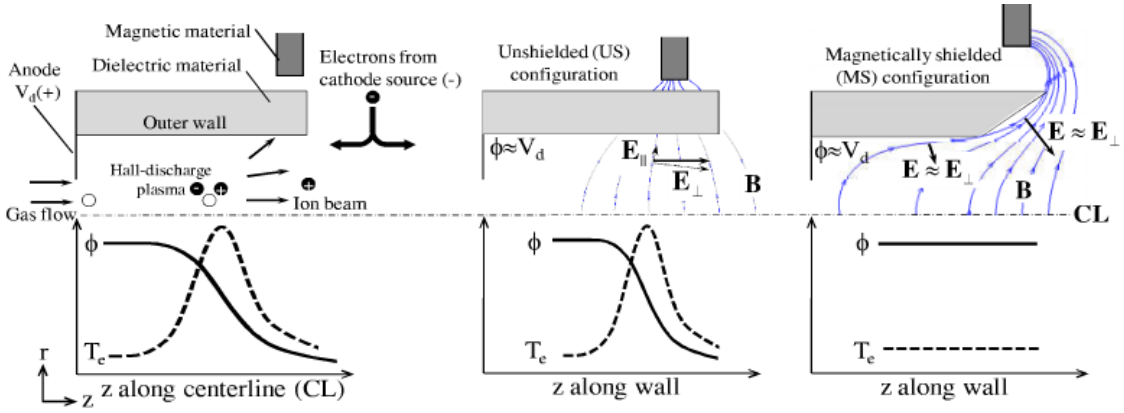

(a) Basic features of the channel (b) Unshielded (c) Magnetically shielded

Figure 1.6 Principle of magnetic shielding [28].

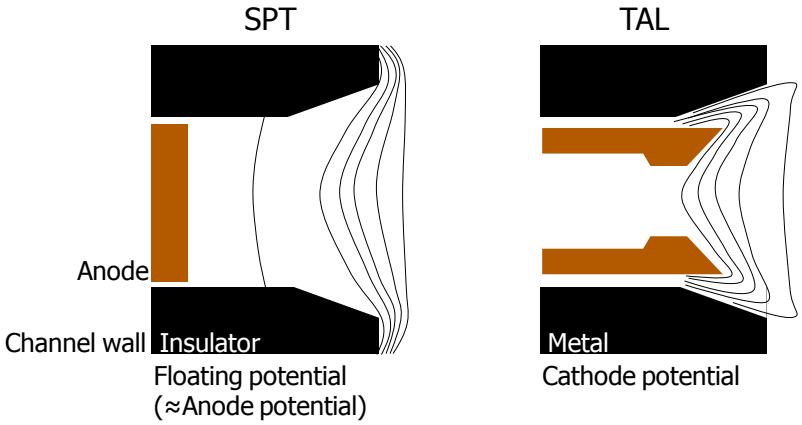

Figure 1.7 Prospective potential contour in a channel of SPT (Left) and TAL (right) with magnetic shield.

1.5 Probe Measurement

To measure the plasma potential and the electron temperature, a probe method would be the best considering its high spatial resolution even inside the channel. There are two plasma diagnosis methods: the probe method and a spectroscopy method. For the probe method, the plasma can be diagnosed by measuring the electrical potential of the probe made of metal inside the plasma or the current flows between the plasma and the probe [30,31]. The plasma diagnosis using the spectroscopy method is done by monitoring the radiation emitted by the plasma and analyzing the obtained spectrum [32].

The probe method has an advantage in its spatial resolution and simplicity, whereas the spectroscopy has better time resolution and less perturbation to the plasma [33]. Although the spectroscopy method has been applied to measure a plume, the plasma outside of the channel, of electric thrusters frequently [34,35,36], there are few application of the spectroscopy method for the measurement inside the channel [37] because the spectroscopy measurement inside the channel requires installation of an inspection window to the channel walls which causes uncertainty to the condition of the plasma. On the other hand, the probe method has been utilized for both the plume [38,39] and the plasma inside the channel [40,41,42,43]. Because of high energy deposition on to the surface of the probe, the plasma inside the channel is measured by inserting the probe from the downstream to upstream parallel to the center axis of the thruster [44].

Among many types of the probes, a floating emissive probe is the most suitable probe for the plasma potential measurement because of its fast response and simplicity [45]. The principle of the floating emissive probe measurement is as follows. In general, if the metal probe is placed inside the plasma, the electrical potential of the floating probe is lower than the plasma potential due to the bigger thermal velocity of the electrons than that of the ions causing the lower electrical potential of the probe to repel the electrons. However, the probe can emit enough amount of thermion to cancel the electron inflow causing the electrical potential of the probe to be the same as the plasma potential when the temperature of the probe is high, which makes it possible to measure the plasma potential just by measuring the floating potential of the probe. The most attractive aspect of using the emissive probe is that the plasma potential can be measured so instantaneously that the observation of the local oscillation of the plasma potential due to the plasma oscillation is possible [46]. Thus, the electric field inside the channel can be obtained by monitoring the floating potential of the probe while the probe is moving inside the channel [47], which is done in this research.

For the electron temperature measurement, a single probe is most suitable because it is possible to detect the existence of the influence which should be removed. The single probe has been widely utilized for the electron temperature measurement [40,48,49]. The electron temperature can be obtained as an inclination of the I-V curve which shows the relationship between the biased probe potential and the natural logarithm of the current that flows from the reference electrode, the cathode

in this research, to the probe. The single probe measurement has an advantage on the detection of distortion due to the magnetic field, an ion beam, and an electron beam, because those influence will appear in the changes of I-V curves [31,50]. Therefore, the electron temperature was measured using the single probe in this research.

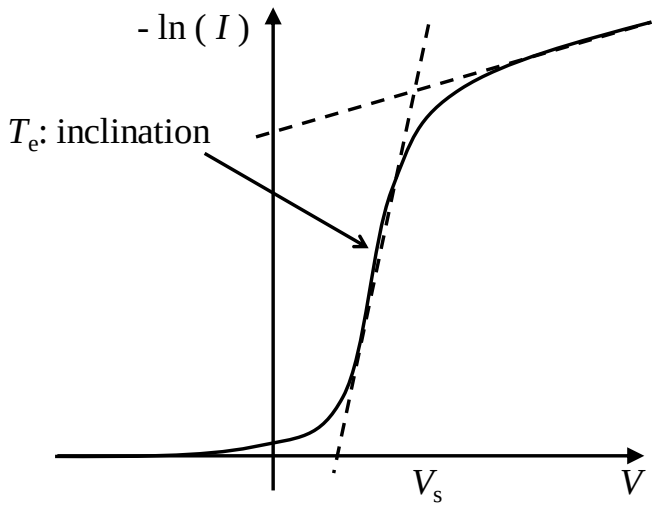

Figure 1.8 Conceptual I-V curve of single probe measurement.

1.6 Motivation of Research

The motivation of this research is to get the criteria for the realization of the zero-erosion TAL by measuring electric field inside the channel of TALs with the geometric configuration of the magnetic shielding and predicting the motion of ions. Because TALs have generally higher thrust efficiency compared to SPTs, the realization of the zero-erosion TAL will enhance the feasibility of in-space transportation of large mass structure. To comprehend the configuration of electric field inside the channel, the axial electron temperature distribution is also measured.

In addition, the derivation of the impact of improvements in the thrust performance on the feasibility of such space mission with large mass is another motivation of this research as well. That result would give an insight about the significantly important performance of Hall thruster, which should be focused on.

1.7 Structure of Thesis

This thesis first describes, in the following chapter, the analysis of the cost for the in-space transportation of a SPS to deduce the specific characteristics of Hall thrusters that will yield significant cost reduction, especially focusing on the impact of the lifetime of Hall thrusters.

The third chapter will describes experimental apparatus for the operation of a Hall thruster and a probe measurement system developed in this research.

The result of the measurement and the discussion is included in the fourth chapter.

Finally, this thesis is summarized in the fifth chapter.

Chapter 2

Mission Analysis of SPS Construction

2.1 Motivation

High-power electric propulsion systems ranging from few to hundreds of kW are actively studied [12,9] in recent years. Electric propulsion systems of this power range can be applied to main thrusters on spacecrafts causing the propellant consumption to be reduced by one order of magnitude. As a result, the space mission capability is enhanced. Satellites recently started to employ 5 kW electric propulsion systems [51], and electric propulsion systems with high power are considered to improve the feasibility of space programs relying on in-space transportation of huge payload such as SPS especially regarding transportation costs [52].

This chapter shows parametric studies of the cost evaluations of in-space transportation of a SPS using Hall thrusters. At first, a base transportation scenario is shown, and then the following section describes the method of cost evaluation. Then, the optimized mission scenario is discussed from the viewpoint of transportation cost by varying the transportation condition parametrically, and finally the specific characteristics are proposed in the last section. This section also describes the quantitative influence of the lifetime on the transportation cost of a SPS.

2.2 Base Transportation Scenario

SPS will be operated in a GEO, a circular orbit 36,000 km above the Earth's equator as exemplarily shown in Figure 2.1. SPS transportation can be divided into two parts as shown in Figure 2.1, the launch from Earth to a LEO, a circular orbit 400 km above ground, and the in-space transportation from LEO to GEO, which is the scope of this study. The usage of OTVs in the in-space transportation was assumed in this study, and the merit of employing OTVs will be discussed in Section 4.1. The OTV was modeled by two major elements; a thruster system and structures. The thruster system includes entire elements which is necessary to operate electric thrusters: thruster head, gimbal, PPU, cabling, propellant feed system, and tank.

To construct a SPS, huge massive structures of several 1,000 to 10,000 tons need to be transported into GEO. This great amount of payload inevitably leads to the employment of separated transfers in individual modules. The SPS mission assumptions used in this study are summarized in Table 2.1. In this study, the transportation cost from LEO to GEO was evaluated to provide a framework of SPS transportation from the viewpoint of costs. In addition, the cost to launch the propellant consumed in this in-space transportation was also evaluated, because the amount of propellant changes depending on the in-space scenario. The target cost for this transportation was assumed to be $3.75 billion (300 million yen), because the entire transportation of SPS has to be accomplished within the expense of $12.5 billion (1 trillion yen) to make it competitive enough compared with other power sources. For the launch vehicle used from the Earth to LEO, H-IIB was assumed. Thus, our evaluation started from the 19 tons of mass supply at LEO, which is the maximum payload of H-IIB [53].

Although there are many candidates for the electric propulsion (EP) system, recent researches [52] show that Hall thruster would be the most promising choice for SPS orbit transfer vehicles (OTVs). Hall thruster has high thrust efficiency, and the specific power, the propulsion power per unit mass, of Hall thruster is also high. Although the desirable power of SEP exceeds 100 kW as will be shown in Section 4.2, clustering of 25 kW thrusters was presumed in this study, because cluster systems would be employed in space programs as a concrete measure against failures.

As propellant for Hall thruster, xenon is usually selected as the ideal candidate to obtain an optimum thrust performance. Xenon is, however, considerably expensive and rare as shown in Table 2.2, and is not a preferable choice for the mass transportation which consumes huge amount of propellant. Therefore, argon was selected as alternative propellant in this study, and, thus, specific impulse was assumed to be 4,000 s. Although the thrust efficiency tends to be lower if argon is employed, the two order of magnitude cost cut compared with xenon can be expected to raise the feasibility of this mission. Taking the use of argon into account, the thrust efficiency was assumed to be 50% at first, and was varied later on as a parameter in order to see the impact of the efficiency on the transportation costs.

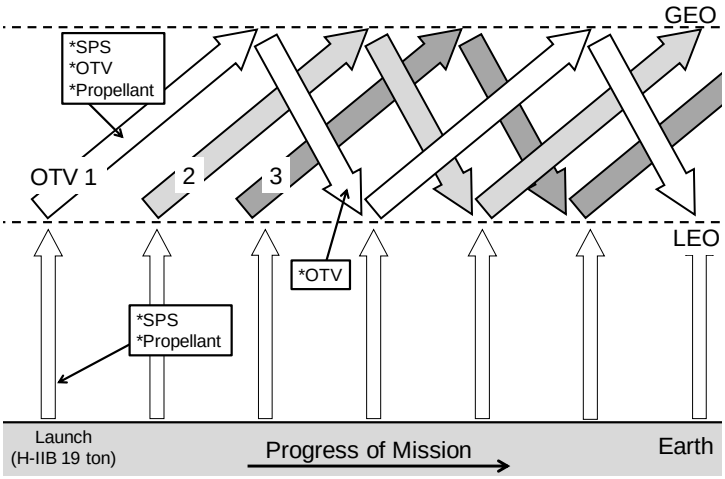

Figure 2.1 SPS transportation scenario.

The number of OTV $N_{vehicle}$ is set to three.

Table 2.1 Requirements of SPS

Weight	20,000 tons
Power output	5 GW
Cost target	Total: $12.5B **LEO to GEO: $3.75B** **(Including propellant launch cost from Earth to LEO)**
Mission period	10 years

Table 2.2 Properties of propellant

	Xe	Kr	Ar
Price $/kg	1,200	330	5
Specific impulse s	2000	3000	4000

2.3 Evaluation Method

To deduce the optimal transportation scenario, several mission cases were evaluated. The total transportation cost is estimated by:

$$C_{\text{total}} = C_{\text{LEO-GEO}} + C_{\text{prop-launch}}. \tag{2.1}$$

The elements of transportation from LEO to GEO can also be divided into two parts from the viewpoint of costs: propellant and OTVs. Thus, in-space transportation cost is estimated by the following equation:

$$C_{\text{LEO-GEO}} = N_{\text{flight}} \cdot c_{\text{prop.}} + N_{\text{vehicle}} \cdot c^{*}_{\text{vehicle}}, \tag{2.2}$$

where c_{prop} is the cost of propellant per unit mass, N_{vehicle} is the number of OTVs necessary to complete transportation within the given mission period. The superscript * indicates the consideration of cost saving along the experience curve. The experience curve is representing the increasing efficiency through the repetitive production. The experience curve is usually expressed by Eq. (2.3) [54], showing a relationship between the production cost and the cumulative production number.

$$c_{\text{vehicle}}(n) = r^{\log_2(n)} c_{\text{vehicle}}(0). \tag{2.3}$$

As Eq. (2.3) shows, when the cumulative production number is doubled, the production cost is multiplied by r. In this paper, r is assumed to be 0.85 with reference to aircraft manufacturing [55]. Thus, the integrated manufacturing cost of OTV is calculated using Eq. (2.4). The impact of repetitive production on cost derived from Eq. (2.4) is shown in Figure 2.2.

$$N_{\text{vehicle}} \cdot c^{*}_{\text{vehicle}} = \sum_{n=1}^{N_{\text{vehicle}}} r^{\log_2(n)} c_{\text{vehicle}}(0). \tag{2.4}$$

The propellant cost is proportional to its mass which is obtained by:

$$m_{\text{prop}} = m_0 \cdot \left\{ 1 - \exp\left(-\frac{\Delta V}{g I_{\text{sp}}} \right) \right\}, \tag{2.5}$$

where m_0 is the initial mass of spacecraft. ΔV is calculated from the Edelbaum's equation [56]:

$$\Delta V = \sqrt{V_{\text{LEO}}^2 + V_{\text{GEO}}^2 - 2 V_{\text{LEO}} V_{\text{GEO}} \cos\left(\frac{\pi}{2} \Delta i \right)}, \tag{2.6}$$

where i is set to 30.4° assuming the launch from Tanegashima, Japan. The calculated velocity increment is ΔV = 6.1 km/s. Using Eq. (2.5) and the ΔV, the mass of propellant necessary for OTV transferring from LEO to GEO was acquired by setting m_0 to the sum of H-IIB payload mass (=19 ton) and OTV dry mass. The propellant mass for the return trip from GEO to LEO is calculated based on the final mass of this flight: OTV mass without propellant.

The OTV cost c_{vehicle} is calculated using two models: one simulates the thruster system cost and the other simulates the structure cost. The thruster system includes thruster heads, gimbals, propellant feed systems, PPUs, a propellant tank and solar array. The structure is a framework to integrate these elements into a single system. The detailed configuration is given in Table 2.3. The cost of thruster systems, which include thruster head, gimbal, PPU, propellant feed system, and tank, is determined by a model [57] obtained by extrapolating the current market prices. The model assumes that the cost of thruster systems would be the function of output power of thruster system as expressed in Eq. (2.7).

$$c_{\text{thruster}}(p) = q \log \frac{p}{p_0} \times c_{\text{thruster}}(p_0) . \tag{2.7}$$

In this model, the constants are set as follows; p_0 = 5 kW and $c_{\text{thruster}}(p_0)$ = \$8 million, and q = 3. The factor q was 2 in the reference [57], though, 3 is employed taking into account the inaccuracy of extrapolating.

The number of round trip between LEO and GEO N_{flight} can be obtained by dividing the total SPS mass by the single modularized SPS mass: the H-IIB payload mass (=19 ton) subtracted by the propellant mass m_{prop} and associated tank mass.

The number of OTV N_{vehicle} is determined from Eq. (2.8) using N_{flight}, transfer orbit duration (TOD) of each flight and entire mission period. This equation represents the scenario when OTVs are utilized most efficiently:

$$N_{\text{vehicle}} = \frac{1}{\frac{\text{Mission Period}}{\text{TOD}}} \cdot N_{\text{flight}} . \tag{2.8}$$

The cost for propellant launch was calculated assuming that the target cost of SPS launch from Earth to GEO of \$8.75 billion was achieved. Thus, $C_{\text{prop-launch}}$ was obtained by:

$$C_{\text{prop–launch}} = \frac{C_{\text{SPS–launch}}}{M_{\text{SPS}}} \cdot M_{\text{prop}} , \tag{2.9}$$

where the target cost of SPS launch $C_{\text{SPS-launch}}$ is \$8.75 billion, M_{SPS} is 20,000 ton, and M_{prop} is the mass of propellant consumed through the entire in-space transportation.

Table 2.3 Breakdown of OTV setup and parameters.

	Mass	Cost
Propellant (argon)	calculated by Eq.(2.5)	$ 5 per 1 kg
Thruster system	-	$15 million per 25 kW
Heads, gimbals, propellant feed system	1.8 kg/kW [52]	
PPUs	1.7 kg/kW [52]	
Tank	4% of propellant mass	
Solar array on OTV	6.0 kg/kW	
Structure	10% of sum of above	$250 thousand per 1 ton

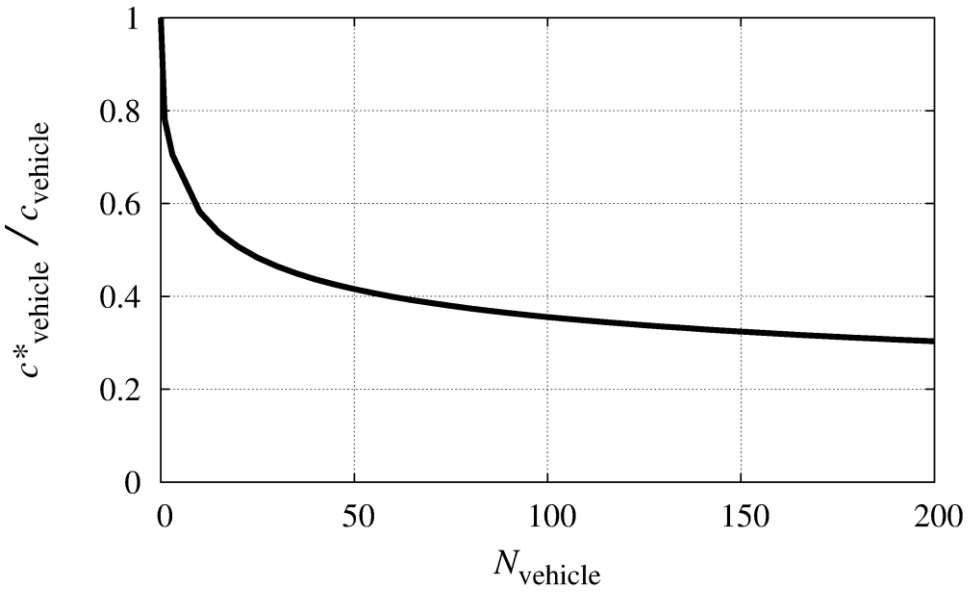

Figure 2.2 Impact of repetitive production on cost assumed in this study.

Cost of single OTV c^*_{vehicle} is normalized by the cost without considering experience curve c_{vehicle}.

2.4 Optimum Scenarios

This section shows the optimum scenarios deduced following the method described in the previous section. Two factors are considered here: the choice of reusing or disposing the OTVs, and propulsion power.

2.4.1 OTV Scenario

A comparative study is conducted to derive which option is better: to restrain the number of OTVs by having them to LEO after unloading the payload at GEO and reuse them; or to avoid the flight back to LEO. In this section, propulsion power is assumed to be 125 kW.

The upper row of Table 2.4 shows the calculation result, where c_{thruster} = \$15 million is the cost of the thruster system derived from Eq. (2.7). The better choice is to reuse OTVs rather than disposing them, as the reusing scenario yields a 74% lower cost of \$5.47 billion.

However, the cost of reusing scenario is still higher than the target cost of \$3.75 billion. In this case, the expense of OTVs' manufacturing cost is as huge as almost 70 % of the total cost as shown in Figure 2.3. Therefore, another cost estimation was conducted assuming the cost of the propulsion system to be low enough so that the total cost could be kept below the target \$3.75 billion. The target cost was achieved as shown in lower row of Table 2.4 when the cost of a 25 kW Hall thruster is reduced to as low as \$7.5 million, half of the value used in the previous estimation. The desirable improvements required for the realization of such a cost-down will be discussed in Section 2.5.

Table 2.4 Cost comparison of two OTV scenarios.

$c_{thruster}$	Scenario	LEO-GEO	Propellant launch	**Total**
$15 million	reusing disposing	$3.84 B $19.7 B	$1.63 B $1.52 B	**$5.47 B** **$21.2 B**
$7.5 million	reusing disposing	$2.09 B $10.6 B	$1.63 B $1.52 B	**$3.72 B** **$12.1 B**

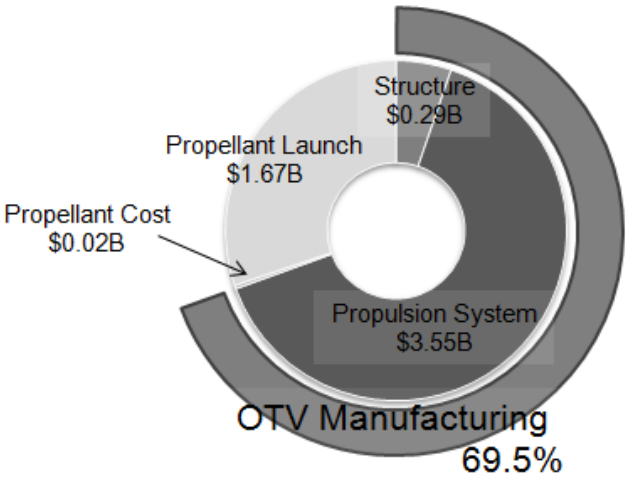

Figure 2.3 Cost breakdown of the reusing scenario.

($c_{thruster}$ = $15 million)

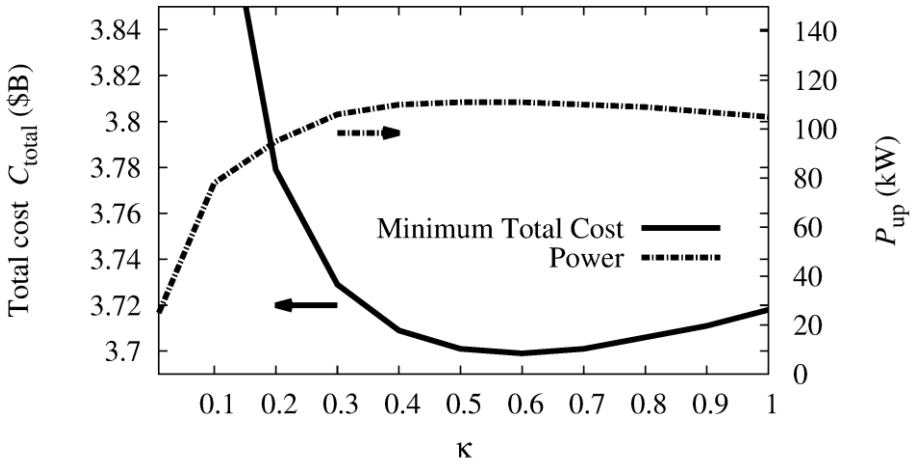

Figure 2.4 Relationship between κ and the minimum total cost (left), and associated P_{up} (right).

κ shows proportion of power contribution from SPS. Eq. (2.10) shows its definition.

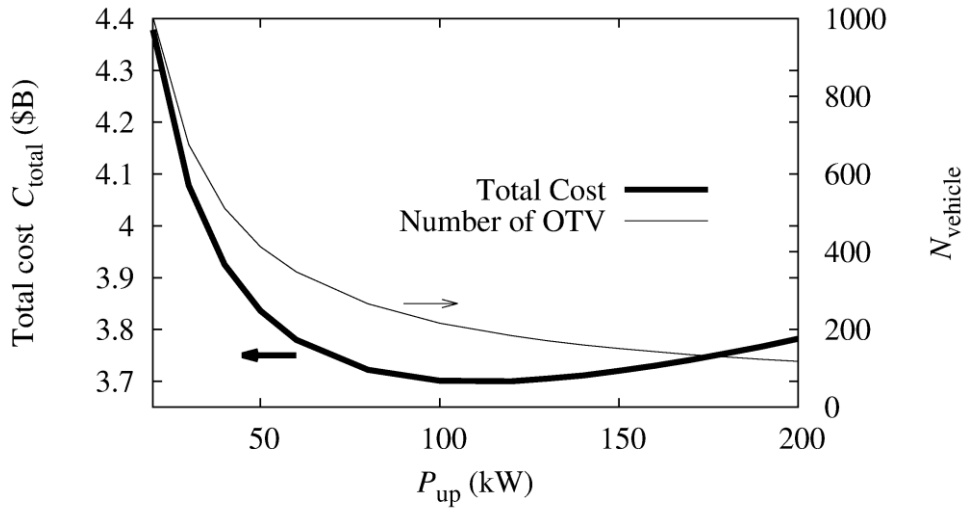

Figure 2.5 Relationship between P_{up} and the total cost (left), and $N_{vehicle}$ (right).

(κ was set to 0.6 considering the result of Section 2.4.2)

2.4.2 Propulsion Power and Power Contribution from SPS

The propulsion power of OTV is another important factor for the cost, because it affects the number of thruster systems and leads to the changes of TOD. This power can be provided by both the OTV's solar array and the SPS module during the transportation from LEO to GEO, whereas the power from the SPS module will no longer be achievable from GEO to LEO. As the mass of solar array is relatively high, the power contribution from the SPS module would reduce the considerable mass and cost. In this section, the optimum propulsion power during the transportation from LEO to GEO P_{up} and the optimum power from GEO to LEO P_{down} which is described using κ,

$$P_{\mathrm{down}} = \kappa P_{\mathrm{up}}. \tag{2.10}$$

Figure 2.4 shows the minimum cost as a function of κ. The minimum point was obtained by evaluating the cost for the wide range of power at each κ. In addition, the power at which the cost yielded a minimum value is also plotted in Figure 2.4 using right ordinate. Small value of κ denotes the expanded use of SPS as the power source to drive OTVs. The remarkable cost increase in the low κ range can be explained by the rapid increase of TOD of return journey. This is because the mass of thruster system for P_{up} - P_{down} = (1 - κ)P_{up} will perform only as dead mass in the transportation from GEO to LEO. It is concluded that the utilization of SPS as power source has little merit.

The relationship between the power and the cost is described in Figure 2.5, where κ was set to 0.6 considering the previous result. P = 112 kW yielded the minimum cost where the effect of decreasing TOD and growing OTV manufacturing cost were balanced. From Figure 2.4 and Figure 2.5, it is clear that as long as the power and κ was set around the favorable value, the cost is not very sensitive to these parameters. However, a power of less than 100 kW should be avoided, because TOD increases drastically with the decrease of the power as described in Figure 2.5. This is important, because a radiation belt exists between LEO and GEO which OTVs would inevitably pass through, and the longer TOD leads to a greater exposure to space radiation hazardous to the SPSs' electric circuits. However, equipment which is strong against space radiation is being developed rapidly [58]. Thus, in order to focus on technologies of Hall thrusters, the effect of space radiation is not considered in this study.

2.5 Specific Characteristics

This section describes the specific characteristics of Hall thruster, which leads to an achievement of target transportation cost of a SPS.

2.5.1 Propellant

In this study, argon has been considered as propellant, because the price of argon is quite low as shown in Table 2.2. However, the current research on use of argon is limited, and the efficiency of Hall thruster with argon still remains unclear. Thus, this section describes the derivation of the influence of both the choice of propellant and the thrust efficiency on the total cost. Three propellants are considered: xenon, krypton, and argon. In this calculation, specific impulses are assumed as shown in Table 2.2.

The result is shown in Figure 2.6. Selecting argon as propellant provides significant cost reduction at a high thrust efficiency range. However, the cost for the case of a thrust efficiency of below 30% with argon exceeds that with krypton. Thus, developing a thruster with a thrust efficiency of more than 30% with argon is desired.

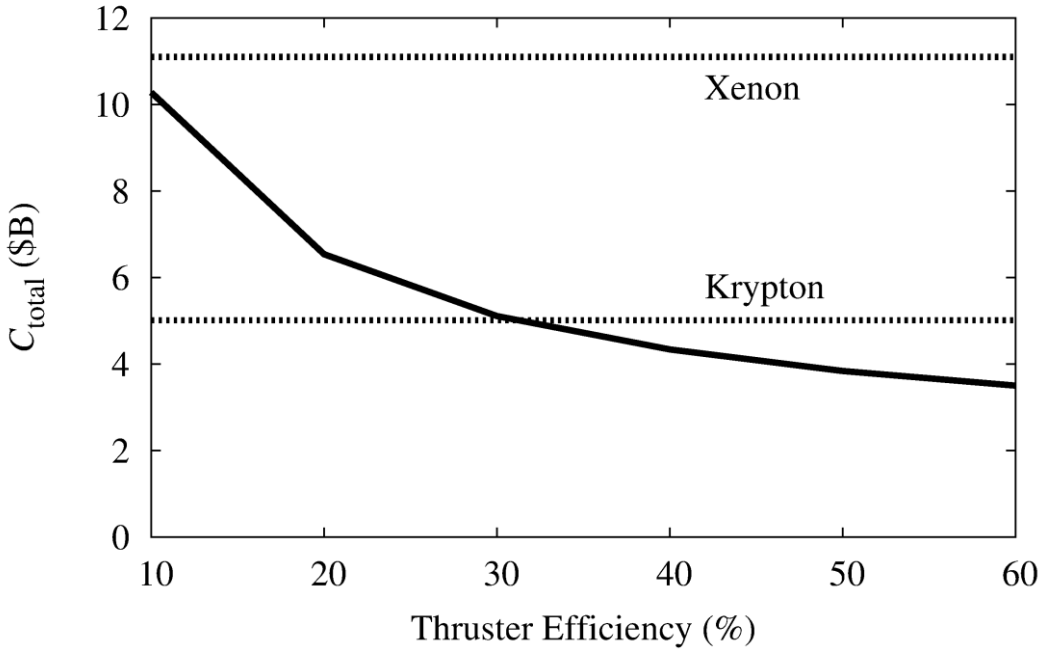

Figure 2.6 Relationship between thrust efficiency and total cost with propellant of argon.

(Thrust efficiency, Kr: 50%, Xe: 60%).

2.5.2 Thrust Efficiency

The impact of thrust efficiency was derived as shown in Figure 2.6. In the case of argon, the result shows that 10% growth in thrust efficiency offers about $400 million cost reduction around efficiency of 50%. As the target cost is $3.75 billion, efforts to improve this efficiency should be conducted to enhance the mission feasibility.

2.5.3 Lifetime

The introduced cost evaluation gives rise to a demand for the reduction of the thruster system manufacturing cost. One of the most effective way to reduce the manufacturing cost is to realize the longer lifetime of the thruster.

The lifetime of Hall thrusters have significant influence on the transportation cost, because the manufacturing cost of thruster systems are high. In this study, the lifetime is assumed to be 10 years considering future innovations related to lifetime. However, if the lifetime were 5 years, the transportation cost would increase by 45%. Therefore, the technologies to increase the lifetime are quite important.

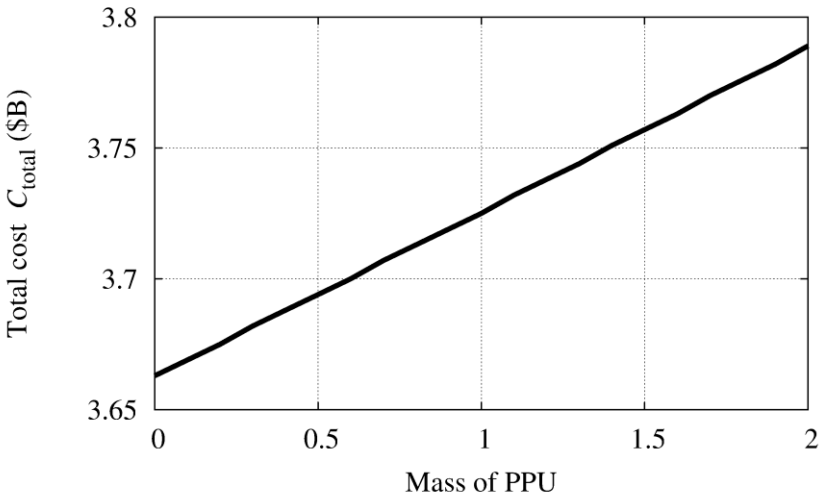

Figure 2.7 Relationship between mass of PPU and total cost.

Mass of PPU was normalized using previously assumed value of 1.7 kg/kW.

2.6 Summary

In-space transportation of a SPS was examined and the following knowledge was obtained, which is also shown in Table 2.5. A better choice of OTV scenario was reusing OTVs rather than disposing them, because the manufacturing cost of OTVs was the dominant part of the expenses, occupying 70% of the total cost. In addition, the power of OTV has limited impact on the total cost, and therefore OTVs can choose its power from a wide range. The fraction of power dependence on SPS during the flight from LEO to GEO yielded no advantage from the viewpoint of cost as described in Section 2.4.2.

The cost of the optimal scenario reflecting this knowledge is shown in Figure 2.3. Based on the results, the specific characteristics of Hall thrusters suitable for in-space transportation of a SPS are presented as follows:

- Capability of operation with argon
- Improved thrust efficiency
- Long lifetime

Table 2.5 Optimum scenario of SPS transportation

(The cost of thruster systems (25 kW) was assumed to be one of fourth of that of the state of the art)

Parameters	Optimum value	Impact on cost
OTV scenario	Reuse OTV	if disposed, cost is 4 times higher
Propellant	Argon	if xenon, cost is 3 times higher
Thrust efficiency	the higher the better	10% eff. improvement, 10% cost reduction
Thrust power	112 kW	small, Figure 2.6
Power contribution from SPS	40% from SPS	small, Figure 2.5

Chapter 3

Experimental Apparatus

3.1 Apparatus for Hall Thruster Operation

3.1.1 Hall Thruster UT-58

In this research, a thruster with anode layer UT-58 developed at the University of Tokyo was tested. A 3D drawing and a picture of UT-58 is shown in Figure 3.1, as well as specifications of UT-58 in Table 3.1.

A magnetic circuit to impress a radial magnetic field in a channel consists of a pole peace, outer cases both made of pure iron (SUYB1). There are two types of solenoid coils used in this thruster: four solenoid coils placed outside of a channel manufactured by winding ceramic insulating magnet wire PIMK-U around coil cases made of copper 160 times, and a solenoid coil placed at the center of the thruster manufactured by winding PIMK-U 320 times. The magnetic field around the channel exit was designed to have mostly radial component along the channel center line, and hollow pure iron parts prevent magnetic field inside the anode from being formed, as shown in Figure 3.2 (a), which was calculated using FEMM 4.2. A magnetic flux density can be varied by controlling a coil current, however, the coil current was set to constantly 2.50 A in this research to measure the electric field with a stable discharge condition of the thruster. Therefore, the magnetic flux density distribution was constant with its maximum magnetic flux density of 55.6 mT, as shown in Figure 3.2 (b).

A channel wall is made of stainless steel (SUS304), and biased at a cathode potential to repel electrons inside the channel keeping an electron temperature inside the channel high.

A plenum chamber was designed to diffuse the propellant azimuthally uniformly before the propellant reaches an anode through 24 small holes (ø1 mm) between them. In addition, to restrain the axial velocity of neutral particles in the channel, and to enhance the azimuthal uniformity of the particles, the channel was designed to be collided at least once by each neutral particle having a change in its diameter in the middle of the channel.

Finally, an ignition sequence is explained here. In general, the operational parameters of Hall thrusters have three degree of freedom: a propellant mass flow rate, a discharge voltage, and a coil current (a magnetic field intensity). In this research, first the mass flow rate and the discharge voltage are set to parameters to measure with the coil current of a relatively higher value, and then, the coil current is reduced gradually until the discharge starts. After the ignition, the coil current is increased gradually to set it to a parameter to measure.

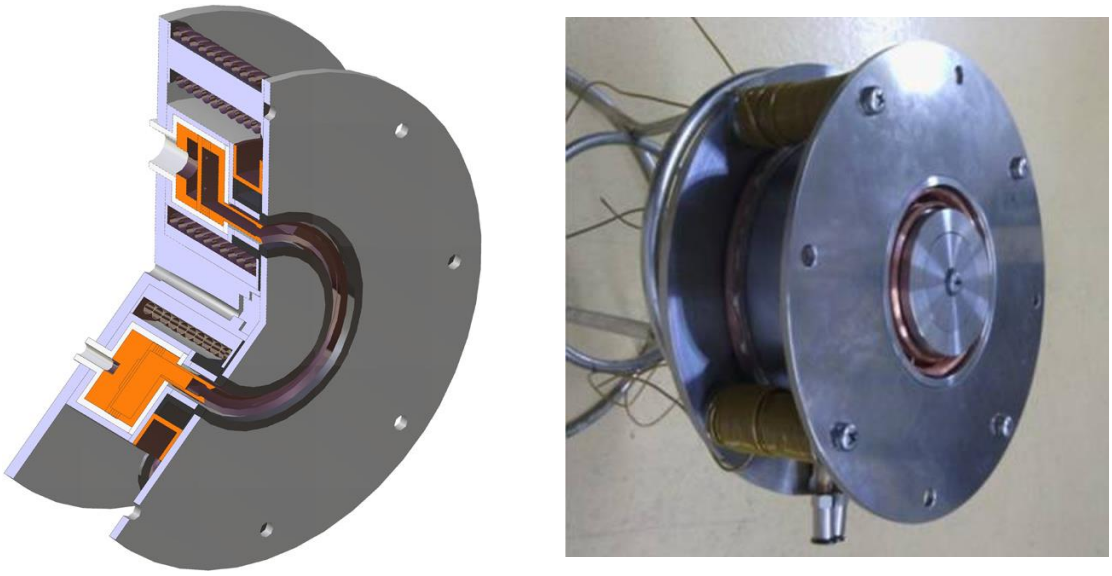

(a) 3D drawing of UT-58　　(b) Picture of UT-58

Figure 3.1　2 kW Hall thruster UT-58 (TAL) developed at the University of Tokyo.

Table 3.1　Specification of UT-58

Anode material	Cupper
Holes for propellant supply	ø 1 mm
Channel outer diameter	ø 66 mm
Channel inner diameter	ø 50 mm
Channel length	2 mm
Insulating material	Alumina
Magnetic circuit material	SUYB1
Magnetic wire	ø 1 mm PIMK-U
Number of turns of windings	160 turns for four outer coils
	320 turns for single inner coils
Cooling medium	Water

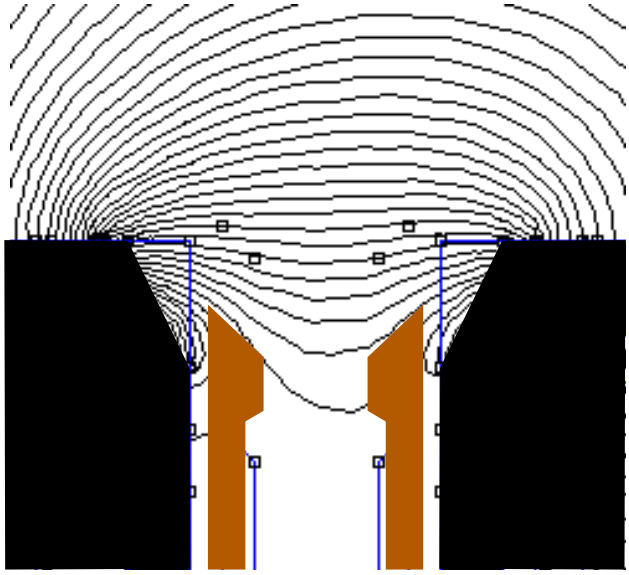

(a) Lines of magnetic force and cross-section schematics.

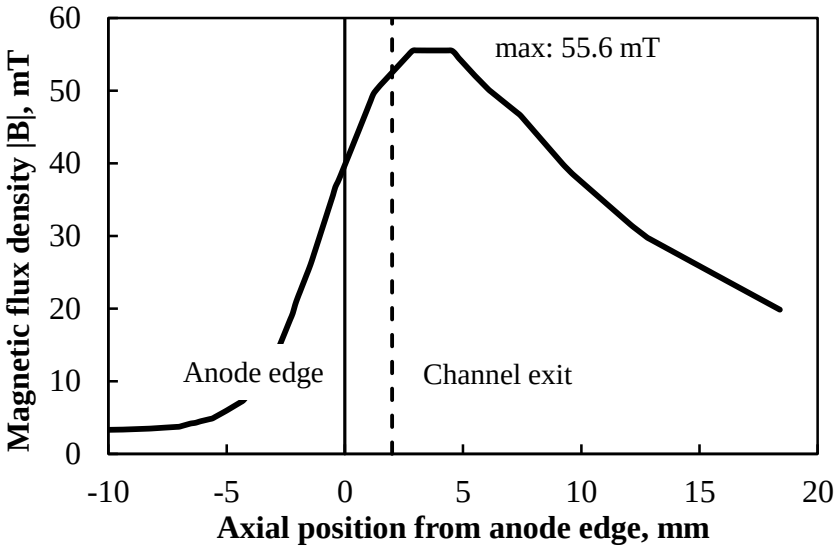

(b) Axial distribution of magnetic flux density along the channel center line.

Figure 3.2 Computed magnetic flux density distribution of UT-58.

3.1.2 Hollow Cathode

A hollow cathode [59] HCN-252 (Veeco Instruments), a tip part of which is shown in Figure 3.3, was used as an electron source during Hall thruster operation. Hollow cathodes are currently the most used electron source for electric propulsions [2]. The hollow cathode has following advantages compared to those other devices: a field emission cathode [60], a microwave plasma cathode [61], a filament cathode.

- Long lifetime (> 1,000 hours)
- Contamination free
- Relatively low energy consumption

Figure 3.4 shows working principle of hollow cathodes. A tantalum foil (an insert) inside a cylinder of the hollow cathode has a layer of low work function R-500 (double carbonate $(Ba/Sr)CO_3$) on its inner surface, so that the insert starts to emit thermions when the temperature of the insert reaches 1,000 degree Celsius in about three minutes after beginning to heat with 7.25 A current. The thermions collide with gas particles generating plasma. The potential difference at the orifice generated by the keeper extracts those generated electrons to outside of the cathode. On the other hand, ions are confined inside the cathode under the influence of double sheath at the orifice of the cathode, and ions recombine with electrons due to the collision with inner wall of the insert. This collision converts ion's kinetic energy into heat energy. The wall accepts the converted heat as well as the heat from the heater. Therefore, the heater current during the operation of the cathode is set to 6 A to avoid overheating.

The following requirements of the hollow cathode were fulfilled throughout this research.

- The cathode is operated with the ambient pressure lower than 2.7×10^{-2} Pa to avoid sputtering erosion of the grid caused by collision of CEX ions or anomalous discharge between the thruster.
- The gas supplied into the cathode is regulated to 99.999% high purity xenon to avoid oxidization of the insert. In addition, the cathode is cooled down for one hour before exposing the cathode to the atmosphere, and during the exposure, argon (20 sccm) is supplied to the cathode to avoid contact of the insert with the atmosphere.
- The cathode is thermally insulated from its support using photoveel and mica sheet to keep the temperature of the cathode high during its operation.

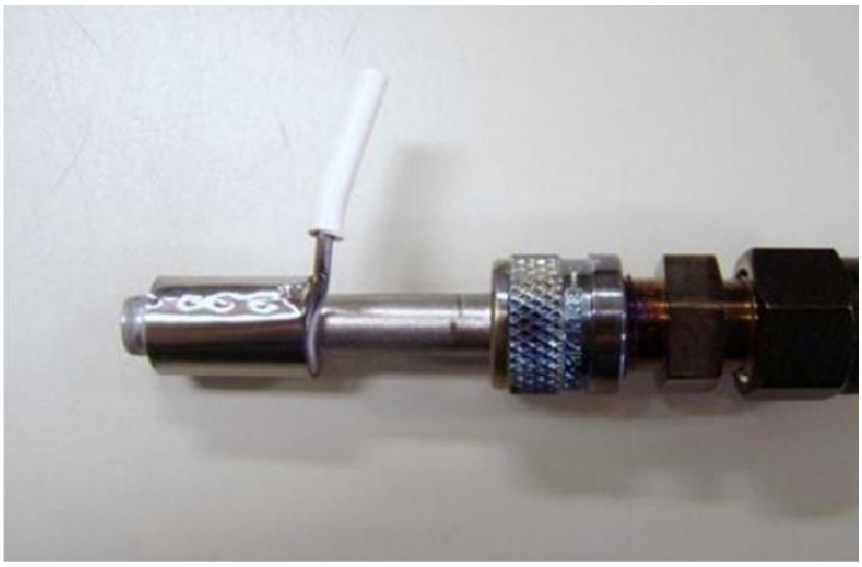

Figure 3.3 A cathode tip of a hollow cathode.

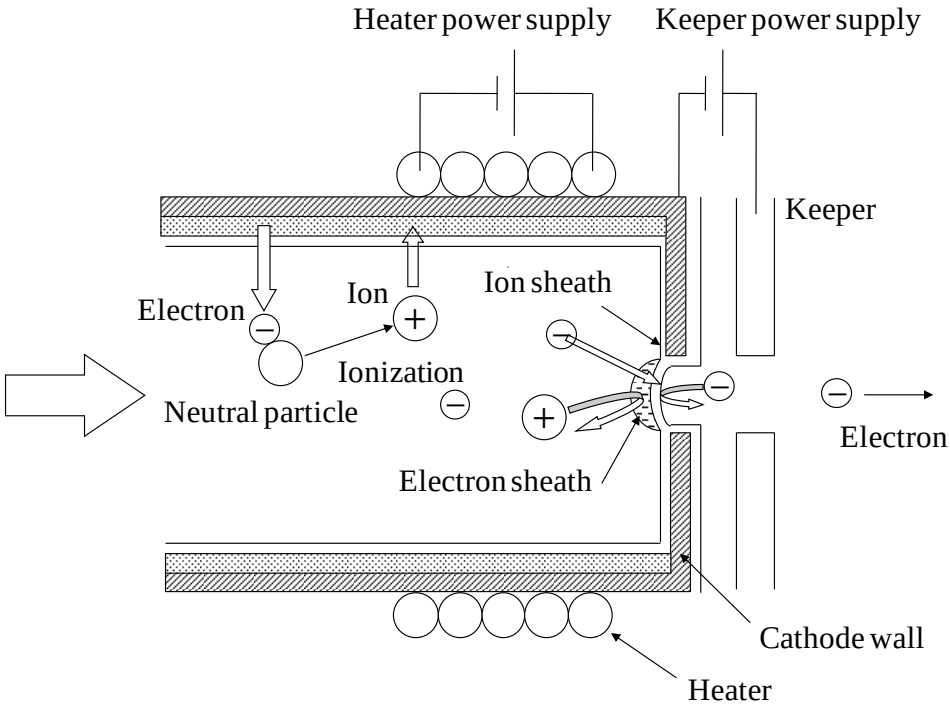

Figure 3.4 Working principle of hollow cathode.

3.1.3 Propellant Feed System

(A) Hongo

The propellant of the thruster and the gas into the cathode are supplied from cylinders of xenon or argon. Regulators attached to the cylinders reduce the pressure to 100 – 200 kPa, and mass flow controllers (Figure 3.5) control flow rate of the gas, which is supplied into the vacuum chamber using 1/4 inch stainless steel pipe. Inside the vacuum chamber, tubes with an outer diameter of 6 mm and an inner diameter of 4 mm are used to supply the gas to the thruster and the cathode. Mass flow controllers MODEL 3200 (KOFLOC) are used for the propellant of the thruster, and MODEL 3660 (KOFLOC) is used for the gas of the cathode. Table 3.2 shows specification of mass flow controllers. These mass flow controllers are operated using read out units MODEL CR-300 (KOFLOC) as shown in Figure 3.6.

Table 3.2 Specification of mass flow controllers (Hongo)

	MODEL 3200	MODEL 3660
S/N	U07010500, U07010510	0607P05213N
Correction of CF	Corrected using xenon	
Valve type	Normally closed, solenoid, diaphragm sheet valve	Normally closed, solenoid, poppet valve
Max. flow rate	50 sccm	20 sccm
Control range	2 – 100%F.S.	2 – 100%F.S.
Accuracy	±1.0%F.S.	±1.0%F.S.
Linearity	±0.5%F.S.	
Repeatability	±0.2%F.S.	±0.5%F.S.
Allowable diff. pressure	49 – 294 kPa	49 – 294 kPa
Leakage rate	smaller than 1×10^{-8} Pa·m^2/s (Permeation of He is not included.)	smaller than 1×10^{-8} Pa·m^2/s (Permeation of He is not included.)

Figure 3.5 Mass flow controllers (Hongo)

Figure 3.6 Read out units of the mass flow controllers (Hongo)

(B) Kashiwa

The propellant is supplied in the same way as in Hongo using different apparatuses. Mass flow controllers SFC1580 (200 sccm, Hitachi metals) are used for the propellant of the thruster, and SFC1580 (20 sccm, Hitachi metals) is used for the gas of the cathode as shown in Figure 3.7. Table 3.3 shows specification of mass flow controllers. These mass flow controllers are operated using read out units FMT1580 (Hitachi metals) as shown in Figure 3.8.

Table 3.3 Specification of mass flow controllers (Kashiwa)

	SFC1580FPYMC-4VL24 (200 sccm)	SFC1580FPYMC-4VL24 (20 sccm)
S/N	7A0421	7A0420
Correction of CF	Corrected using xenon	Corrected using xenon
Valve type	Normally closed, piezo actuator, metal diaphragm sheet valve	Normally closed, piezo actuator, metal diaphragm sheet valve
Max. flow rate	200 sccm	20 sccm
Control range	2 – 100%F.S.	2 – 100%F.S.
Accuracy	±0.5%F.S.	±0.5%F.S.
Linearity	±0.3%F.S.	±0.3%F.S.
Allowable diff. pressure	0.05 – 0.3 MPa	0.05 – 0.3 MPa
Leakage rate	smaller than 1×10^{-11} Pa·m^3/s (He)	smaller than 1×10^{-11} Pa·m^3/s (He)

Figure 3.7 Mass flow controllers (Kashiwa).

Figure 3.8 Read out units of the mass flow controllers (Kashiwa).

3.1.4 Electrical circuits

(A) Hongo

Figure 3.9 shows an electrical diagram of the power supply system in Hongo. A resistor for measurement of the discharge current and a fuse for overcurrent protection are connected in series between a positive terminal of the main discharge power supply and the anode of the thruster. For the resistor for measurement of the discharge current, fixed metal film resistors are used taking account of their high frequency characteristic of 100 MHz, their small thermal noise, and their small temperature coefficient of resistance. The resistance is 0.5 Ω, and power rating of them is 60 W. The discharge current was measured by monitoring a potential difference between the two ends of the resistors using a differential probe. For the discharge voltage measurement, a potential difference between the point immediately after the anode of the thruster and a negative terminal of the main discharge power supply using another differential probe. The influence of the differential probes on the discharge is negligible, because an input impedance of the differential probe of around 3 MΩ is much greater than an equivalent resistance of a Hall thruster of around 100 Ω. A fixed metal film resistor with resistance of 0.5 Ω and power rating of 20 W is connected in series between the body of the thruster and a negative terminal of the main discharge power supply to measure the guard ring current.

Vacuum current feedthroughs are used for electrical connection between the inside and outside of the vacuum chamber, such as power supply for the thruster, measurement of a probe current, and signal transferring of sensors.

Pictures of DC regulated power supplies used in this research are shown in Figure 3.10, and rated values of them are shown in Table 3.4.

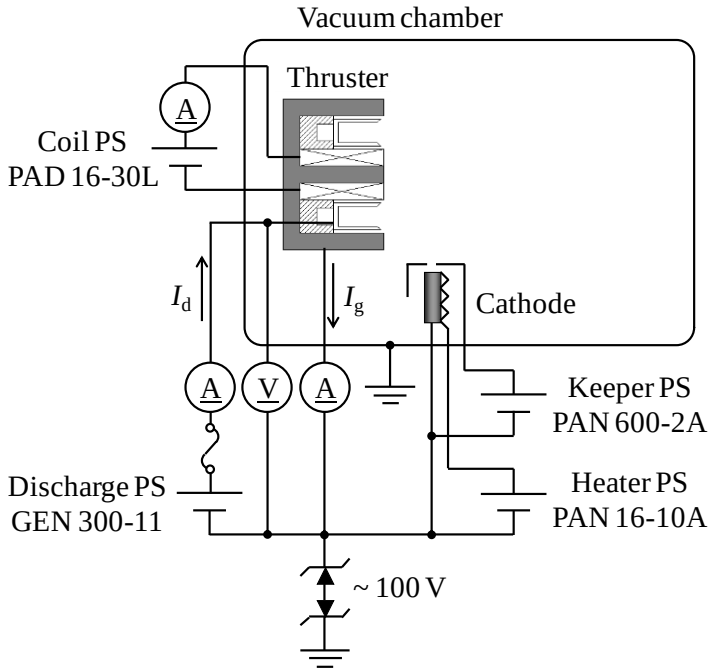

Figure 3.9 Electrical diagram of the power supply system (Hongo).

Table 3.4 Rated values of power supplies (Hongo)

Application	Model number	Manufacturer	Rated value
Main discharge	GEN 300-11	TDK Lambda	300 V – 11.0 A
Coils in the thruster	PAD16-30L	Kikusui	16 V – 30.0 A
Heater of the hollow cathode	PAN16-10A	Kikusui	16 V – 10.0 A
Keeper of the hollow cathode	PAN600-2A	Kikusui	600 V – 2.0 A

(a) Main discharge

(b) Heater of the cathode

(c) Coil of the thruster

(e) Keeper of the cathode

Figure 3.10 Power supplies (Hongo).

(B) Kashiwa

Figure 3.11 shows an electrical diagram of the power supply system in Kashiwa. Fixed metal film resistors are used for measurement of the discharge current, the resistance of which is 0.5 Ω, and power rating of them is 60 W. Differential probes are used to monitor the discharge current and the discharge voltage in the same way as in Hongo. A fixed metal film resistor with resistance of 0.5 Ω and power rating of 20 W is used to measure the guard ring current.

Pictures of DC regulated power supplies used in this research are shown in Figure 3.12, and rated values of them are shown in Table 3.5.

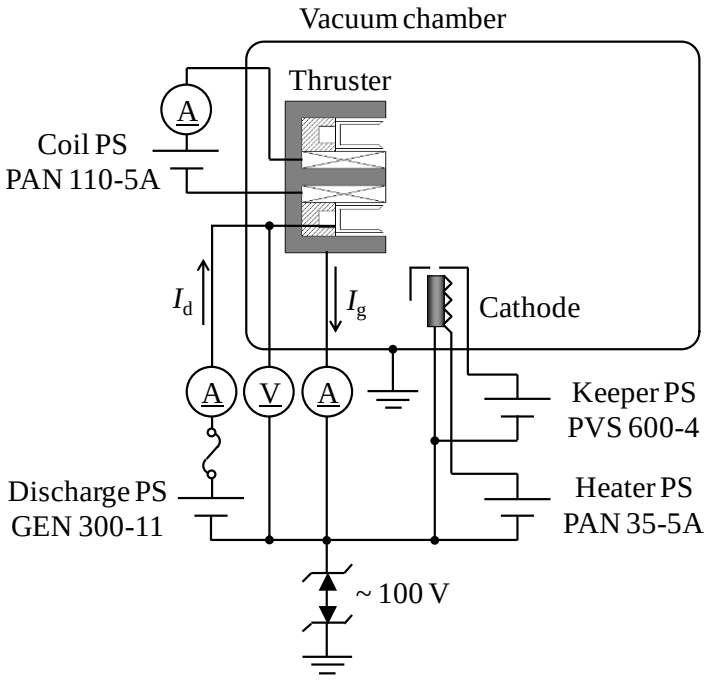

Figure 3.11 Electrical diagram of the power supply system (Kashiwa).

Table 3.5 Rated values of power supplies (Kashiwa)

Application	Model number	Manufacturer	Rated value
Main discharge	GEN 300-11	TDK Lambda	300 V – 11.0 A
Coils in the thruster	PAN110-5A	Kikusui	110 V – 5.0 A
Heater of the hollow cathode	PAN35-5A	Kikusui	35 V – 5.0 A
	(Two sets in parallel)		(35 V – 10.0 A)
Keeper of the hollow cathode	PVS 600-4	Kikusui	600 V – 4.0 A

(a) Main discharge

(b) Heater of the cathode

(c) Coil of the thruster

(d) Keeper of the cathode

Figure 3.12 Power supplies (Kashiwa).

3.1.5 Vacuum System

(A) Hongo

To simulate the vacuum environment, a large vacuum chamber SSC-2000 (ULVAC, stainless steel, Diameter: 2.0 m, Length: 3.0 m, Volume: 10 m^3) is used as shown in Figure 3.13. For the vacuum pumps, three types of pumps are used: an oil diffusion pump SPD-36 (ULVAC, Pumping speed: 37,000 L/s) as a primary pump directly connected to the chamber, a mechanical booster pump PMB-060B (ULVAC, Pumping speed: 1,720 L/s) as a second pump connected to the primary pump in series, and dual rotary pumps PKS-070 (ULVAC, Pumping speed: 115 L/s) as third pumps. These vacuum system including valves is controlled using a single control unit. Appearance of these pumps and the control unit are shown in Figure 3.14.

For the measurement of the pressure inside the vacuum chamber, two types of vacuum gauges are used: a Pirani gauge GP-1S (ULVAC, Gauge head: WP-02) for low vacuum of atmospheric pressure to 1.0×10^{-1} Pa and an ionization gauge GI-TL2 (ULVAC, Gauge head: W1-T15) for the higher vacuum. The ionization gauge requires sensitivity calibration depending on the gaseous species. A relative sensitivity factor of xenon gas is 2.5.

Figure 3.13 A large vacuum chamber (Hongo).

(a) An oil diffusion pump

(b) A mechanical booster pump

(c) Dual rotary pumps

(d) A control unit

Figure 3.14 Vacuum pumps and control unit (Hongo).

(B) Kashiwa

A vacuum chamber MB94-1066 (ULVAC, stainless steel, Diameter: 1.4 m, Length: 3.0 m, Volume: 10 m^3) is used as shown in Figure 3.15. For the vacuum pumps, two types of pumps are used: dual cryopumps Cryo-U20P (ULVAC, Pumping speed for nitrogen: 10,000 L/s) and SA-18T (Suzuki shokan, Pumping speed for nitrogen: 8,000 L/s) as a primary pump directly connected to the chamber and a rotary pump KRP-3000 (DIAVAC, Pumping speed: 50 L/s) as a roughing pump. The appearance of these pumps and the control unit are shown in Figure 3.16.

For the measurement of the pressure inside the vacuum chamber, two types of vacuum gauges are used: a Pirani gauge PT-3DA (DIAVAC, Gauge head: PSG-1) for low vacuum of atmospheric pressure to 13 Pa and an ionization gauge M-431HG (CANON ANELVA TECHNIX, Gauge head: MG-2) for the higher vacuum. The ionization gauge requires sensitivity calibration depending on the gaseous species. A relative sensitivity factor of xenon gas is 2.5.

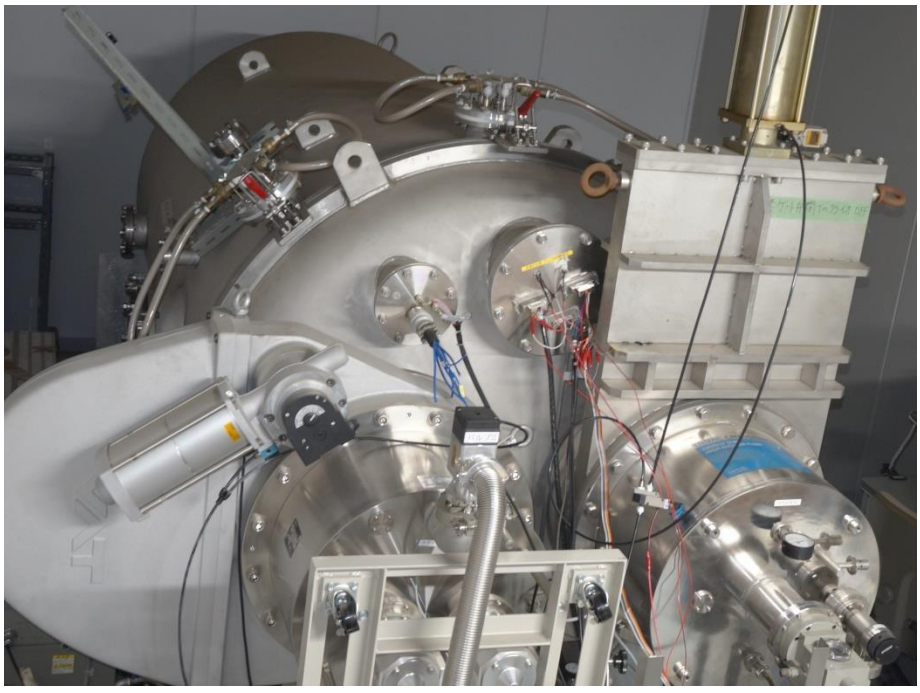

Figure 3.15 A vacuum chamber (Kashiwa).

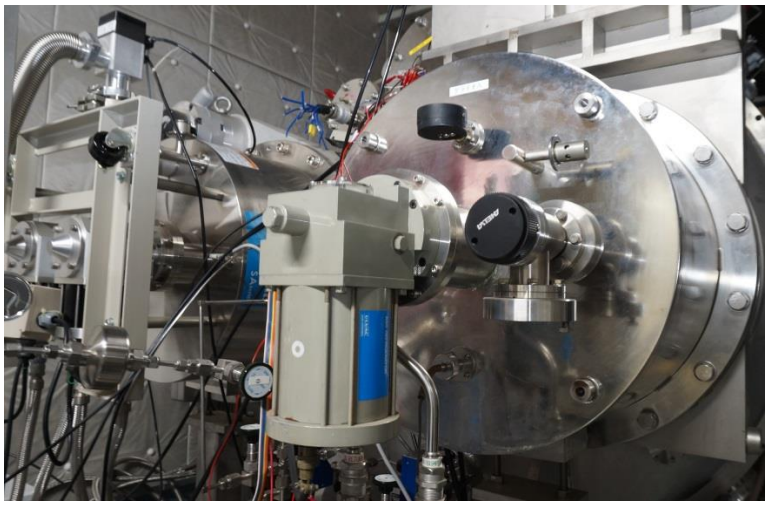

(a) Dual cryopumps SA-18T and Cryo-U20P

(b) A compressor for SA-18T

(c) A compressor for Cryo-U20P

(b) A rotary pump

(c) A control unit with vacuum gauges and a thermometer

Figure 3.16 Vacuum pumps and control unit (Kashiwa).

3.2 Apparatus for Probe Measurement

3.2.1 Emissive Probe

The plasma potential was measured using an emissive probe, an instantaneous measurement device for the plasma potential. The dimension and picture of the emissive probe used in this research is shown in Figure 3.17. The electrode to measure the plasma potential was a filament, the diameter of which is 0.15 mm, and a filament current of 3.20 A was fed to the filament to heat the electrode using a power supply PAN16-10A (Kikusui, 16 V – 10.0 A). This is because the floating potential saturated with the filament current of 3.20 A as the filament current was increased, as shown in Figure 3.19. To enhance the axial spatial resolution, the distance of the tip of the electrode from the insulating tube was regulated up to 0.5 mm.

For the insulating tube, an elliptical alumina tube having the transverse diameter of 3.0 mm and the conjugate diameter of 1.5 mm was used. The probe was fixed so that the minor axis cross the channel walls perpendicularly to maximize the radial measurement range. This insulating tube was covered with a stainless tube staring from the 25 mm downstream of the electrode to enhance the positioning accuracy of the probe by strengthen the probe. The insulating tube was fixed to the stainless tube using low vapor-pressure epoxy resin sealant Torr Seal (Varian).

The floating potential was measured as the voltage difference between the electrode and the cathode using a differential probe. To correct the influence of the potential gradient at the filament, the output voltage of the power supply for the filament was added to the measured floating potential. The obtained sample was smoothed using a digital filter and averaged for the five smoothed data to obtain a reasonable electric field as shown in Figure 3.20. The positioning accuracy was confirmed to be quite high, because the sample obtained by moving the probe from outer to inner of the thruster is almost the same as that of inner to outer motion, as shown in Figure 3.20.

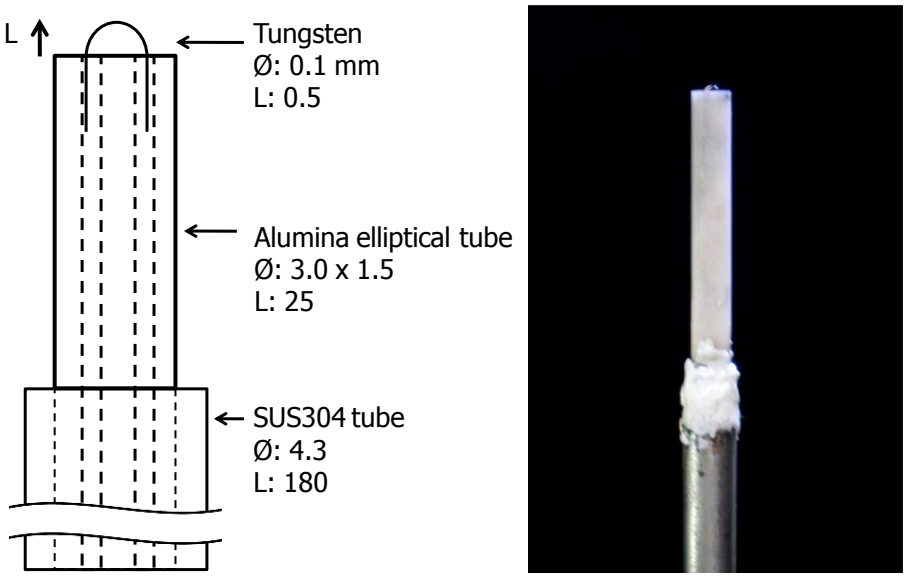

Figure 3.17 Dimension of an emissive probe (left) and its picture (right).

Figure 3.18 A power supply for the filament of an emissive probe.

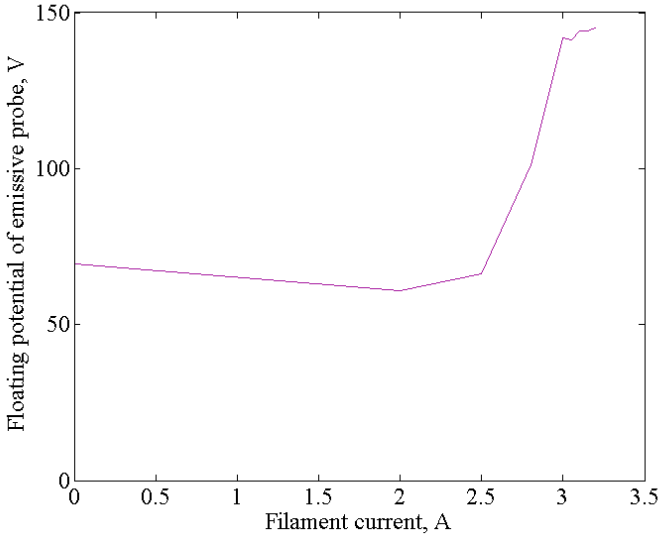

Figure 3.19 Relationship between filament current and floating potential of emissive probe.

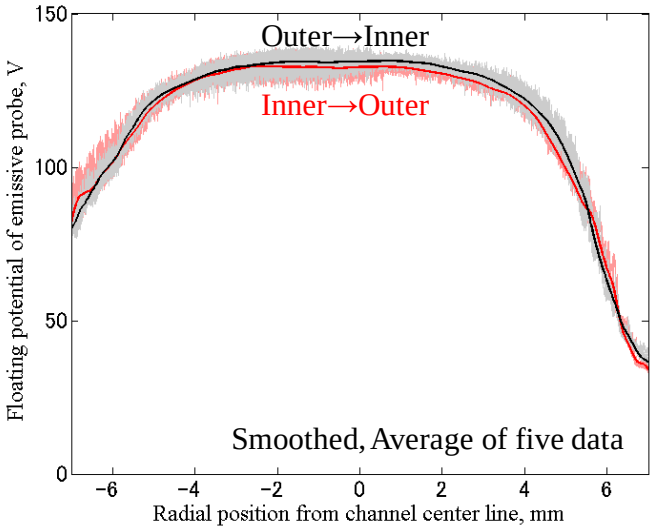

Figure 3.20 Typical sample of the radial plasma potential distribution of the emissive probe.

3.2.2 Single Probe

Single probe measurement was conducted to obtain an electron temperature distribution. The dimension and picture of the single probe is shown in Figure 3.21. The diameter of the electrode is 0.1 mm and the length is 1.0 mm, so that the length of the probe is bigger enough compared to the diameter. This is because the existence of magnetic field parallel to the probe surface around the measurement point has a negative influence on the I-V curves to measure the electron temperature from the inclination of the I-V curve [62], as shown in Figure 3.22. The electrode was covered by two different diameter cylindrical tubes and a stainless tube, and these tubes were fixed using Torr Seal.

The electrical diagram for the measurement of the current of the probe is shown in Figure 3.23, as well as the picture of the electric circuit in Figure 3.24. As Figure 3.23 (a) shows, the bias voltage control part consists of two elements: a power supply for biasing the voltage of the electrode PMC250-0.25L (Kikusui, 250 V – 0.25 A, Figure 3.25) and a switch SS-1A 05DM (Shoi electric). The output voltage of the power supply was controlled using a LabVIEW program, which also controls the motion of the motors, so that the voltage biasing and the positioning of the probe works together. The switch is installed to keep the electrode floated during the motion of the probe, because the floating potential of the probe changes so rapidly during the motion that it is impossible to control the biased voltage corresponds to that change. This switch is also controlled using the LabVIEW program.

For the current measurement, the voltage difference between two ends of a 20 Ω resistor was monitored as shown in Figure 3.23 (b). To measure the wide range of the voltage difference accurately, which ranges from around 0.1 mA to 250 mA, a logarithmic amplifier LOG112 (Texas Instruments, 5 decades measurement range) was used. The biased voltage was measured at a point between the resistor and the probe using a differential probe. To reduce the error of any ICs outputs due to the signal oscillation, passive filters (f_c = 16 kHz) were installed between the measurement points and the ICs. The sampling frequency of the single probe measurement is 5 kHz; therefore the filter does not change the sampled data.

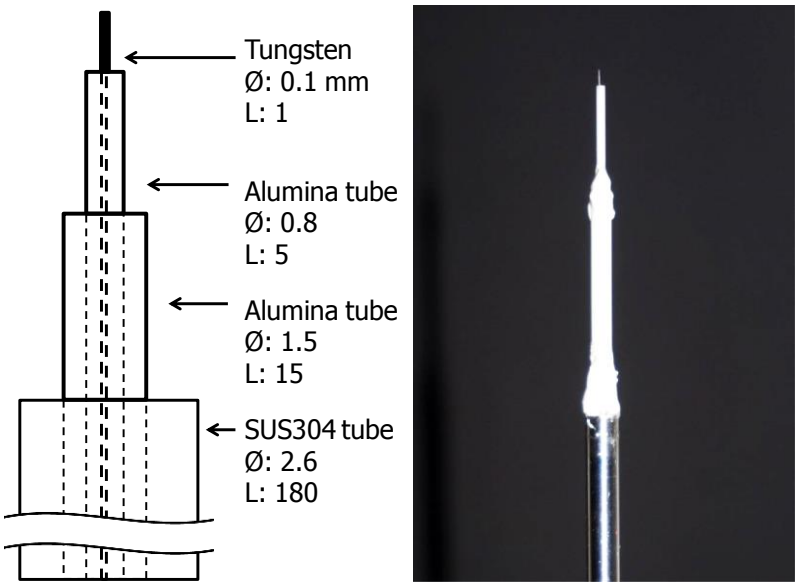

Figure 3.21 Dimension of a single probe (left) and its picture (right).

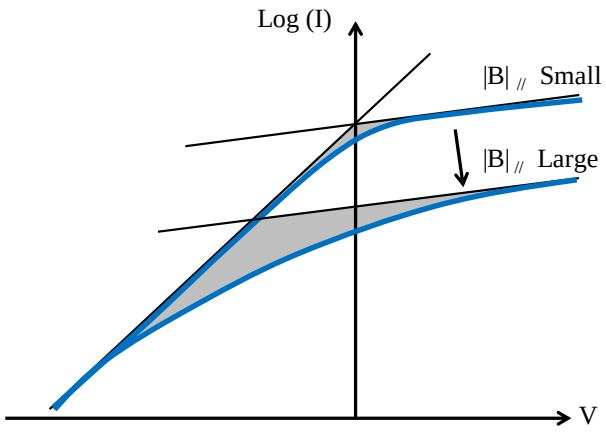

Figure 3.22 Conceptual diagram of I-V curves obtained both in small/large magnetic flux density parallel to the probe [62].

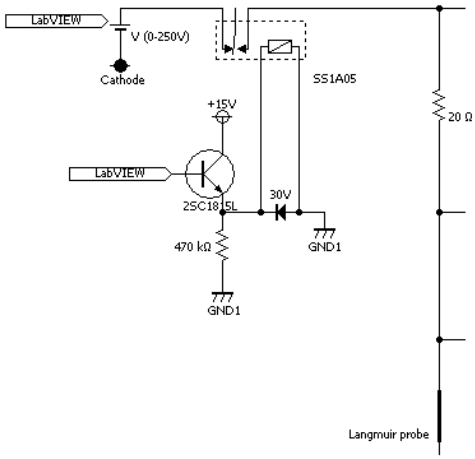

(a) Biase voltage control part

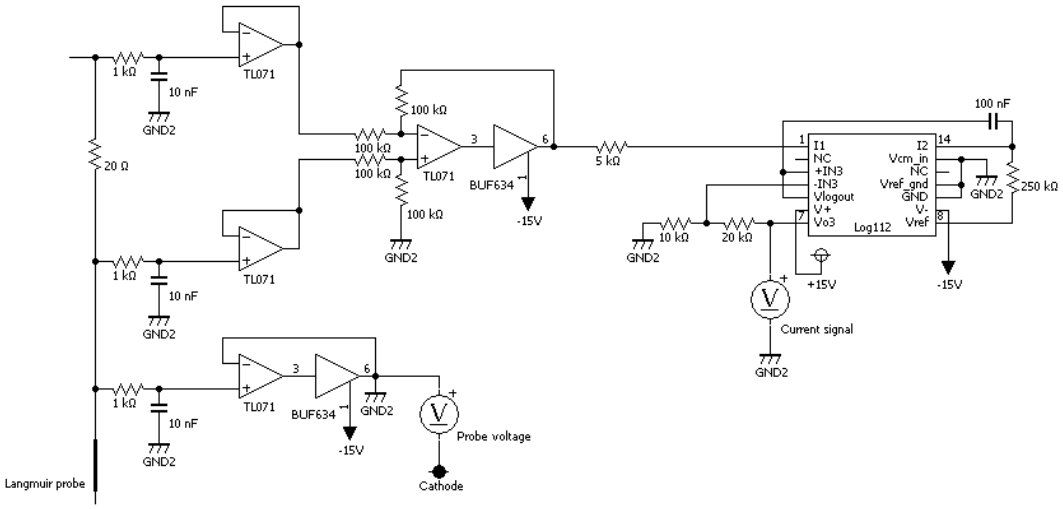

(b) Current and voltage measurement part

Figure 3.23 Electrical diagram for the single probe measurement.

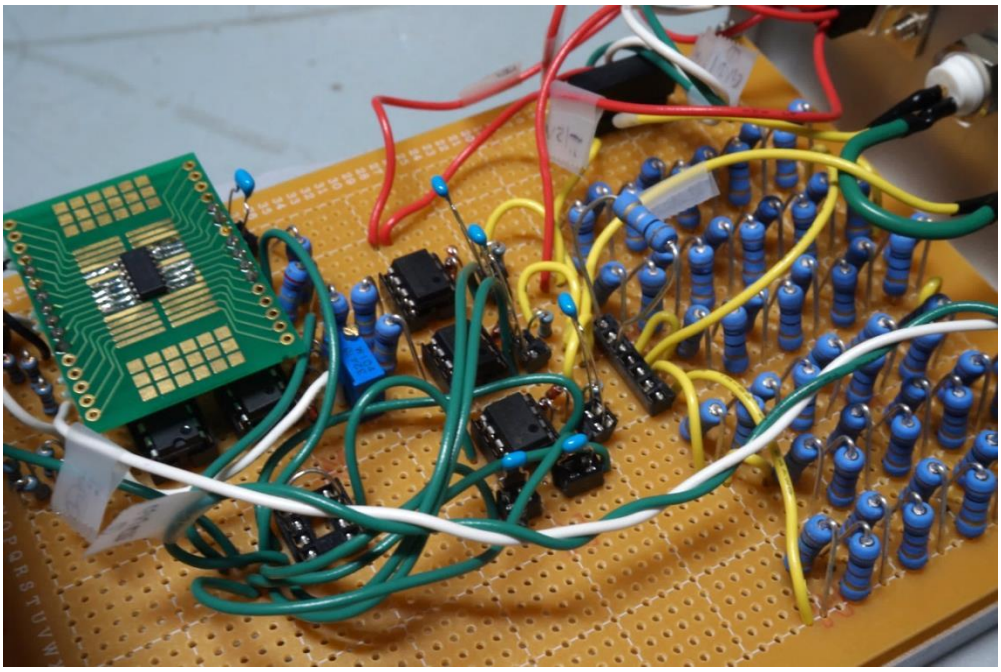

Figure 3.24 Picture of electric circuit for single probe measurement.

Figure 3.25 Power supply for single probe voltage biasing.

Chapter 4

Experimental Results

4.1 Channel Wall Loss

The channel wall loss of UT-58 was measured and compared with a thruster without the channel wall geometric configuration of a magnetic shielding, UT-38. To evaluate the channel wall loss, the guard ring current was measured for UT-58 to obtain the ratio of ion loss current and the discharge current $\varepsilon_{\text{ion-wall}}$, which is defined by Eq.(4.1).

$$\varepsilon_{\text{ion-wall}} \equiv \frac{I_{\text{g}}}{I_{\text{d}}} = \frac{I_{\text{g}}}{I_{\text{b}} + I_{\text{e}} + I_{\text{g}}}, \tag{4.1}$$

where, I_{g} is a guard ring current and I_{d} is a discharge current. During the measurement of a guard ring current, the front surface of the thruster was covered with boron nitride (BN) powder to prevent the ions from flowing into the thruster from the front surface, as shown in Figure 4.1 and Figure 4.2. Insulating the thruster surface is effective for cancelling the current due to the charge exchange (CEX) ions, which increases a guard ring current considerably [63]. The thruster was operated with the following conditions: the discharge voltage of 150 V, the xenon mass flow rate of 1.95 mg/s (20.0 sccm, 1.43 $A_{eq.}$), and the maximum magnetic flux density of 55.6 mT (Coil current of 2.50 A). For UT-38, the ion energy loss ratio toward the wall $\varepsilon_{\text{ion-wall}}$ was derived from the previous study with the operating conditions: the discharge voltage of 250 V, the xenon mass flow rate of 2.04 mg/s (20.9 sccm, 1.50 $A_{eq.}$), and the maximum magnetic flux density of 51.0 mT.

The $\varepsilon_{\text{ion-wall}}$ of UT-58 is 3.8%, 60% smaller than $\varepsilon_{\text{ion-wall}}$ of UT-38 (9.6% [63]).This result shows that the ion loss toward the wall of UT-58 (with magnetic shield) is small compared with UT-38 (without magnetic shield). Therefore, the channel wall erosion of UT-58 can be inferred to be reduced due to the installation of geometric configuration of magnetic shielding. To verify the effect of the geometric configuration of magnetic shielding with TAL on the reduction of the channel wall erosion, however, investigation of the ion motion inside the channel by measuring the electron temperature distribution for the detection of the approximate ionization region and the electric field for the estimation of the ion trajectory is inevitable.

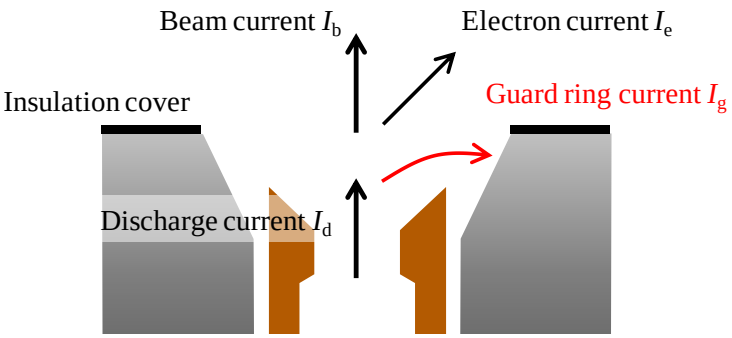

Figure 4.1 Channel wall erosion rate measurement method.

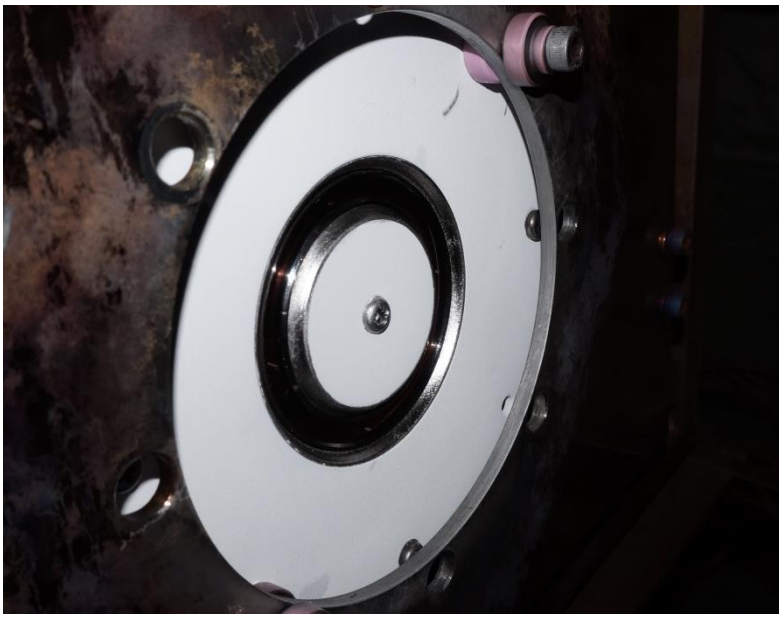

Figure 4.2 Picture of the thruster covered its front surface with boron nitride powder.

4.2 Axial Electron Temperature

An axial electron temperature distribution was measured to estimate the ionization region inside the channel, which is necessary to discuss about the ions flowing into the channel wall. An electron temperature is one of the physical quantities to determine the ionization rate: an electron number density, a neutral number density, and an electron temperature. Figure 4.3 shows the axial electron temperature distribution and computed magnetic flux density along the channel center line. The electron temperature inside the hollow anode is low ranging from 3.5 to 7 eV at every point. As the axial position increases, the electron temperature increases sharply, and it takes its peak value of 18 eV at the channel exit plane (2 mm of the axial position from the anode edge). The electron temperature decreases rapidly as the position moves toward the outside until around 8 eV at 5 mm of the axial position from the anode edge, and the electron temperature takes a constant value of around 8 eV from 5 to 20 mm of the axial position.

Although it is necessary to have the three physical quantity distribution to determine the ionization region properly, it can be inferred from this electron distribution that the ionization takes place mainly in the region from 1 to 3 mm of the axial position. Therefore, the target area of the following electric field measurement inside the channel was set to this area.

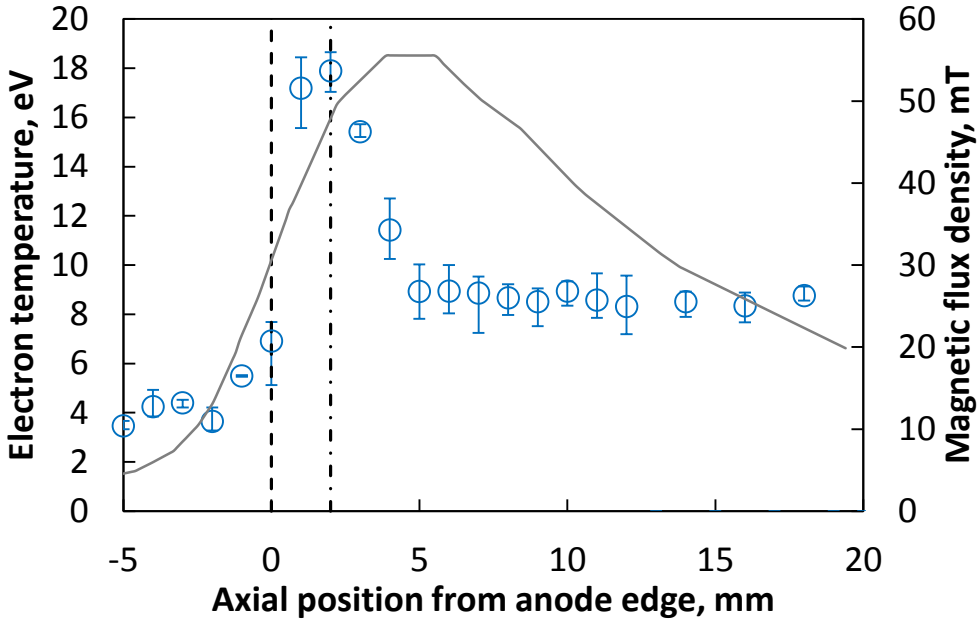

Figure 4.3 Electron temperature distribution along the channel center line.

(V_d = 150 V, $\dot{m}$ = 2.72 mg/s, $|\boldsymbol{B}|$ = 55.6 mT)

4.3 Axial Potential Distribution

To detect the ion acceleration region, the axial potential distribution was measured using an emissive probe. The measurement was done while the axial position of the probe was shifted with the reciprocating motor, and then the obtained signal history was converted to the axial distribution. The distribution was then smoothed by using a finite impulse response (FIR) filter, five datasets of which were averaged to enhance the reliability of the data. Figure 4.4 shows the axial potential distribution with the discharge voltage of 150 V, the xenon mass flow rate of 1.95 mg/s (20.0 sccm, 1.43 $A_{eq.}$), and the maximum magnetic flux density of 55.6 mT (Coil current of 2.50 A). The potential inside the anode is around 150 V, and it drops to around 30 V at 50 mm of axial position from anode edge. The ions generated around the anode are accelerated by this potential difference, and as the most dominant potential drop exists in a regulated region starting from axial position of 0 to 10 mm from anode. Therefore, the following electric field measurement was conducted between these two points.

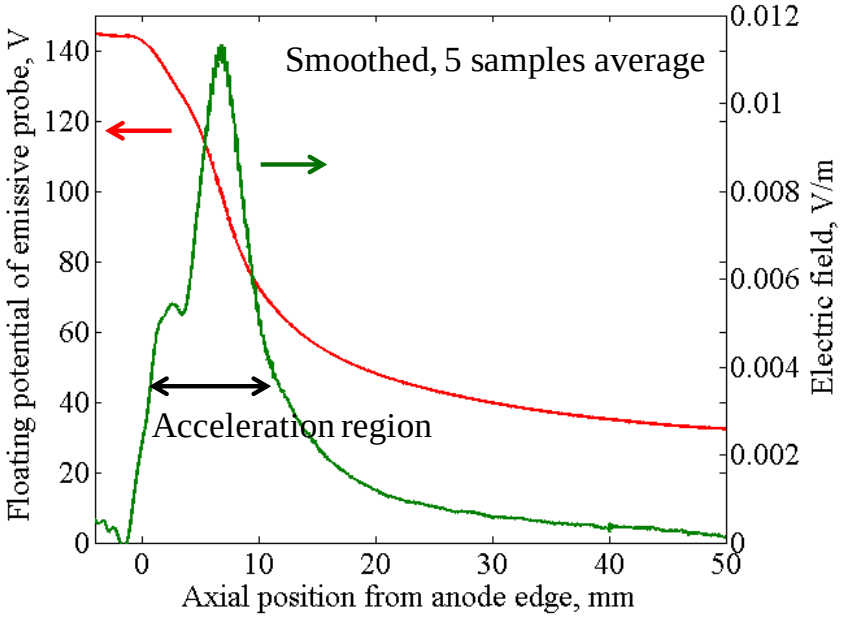

Figure 4.4 Axial potential distribution (Filament of 3.2) with averaging and filtering.

(V_d = 150 V, $\dot{m}$ = 1.95 mg/s, $|\boldsymbol{B}|$ = 55.6 mT)

4.4 Electric Field

4.4.1 Acceleration Region

Figure 4.5 (a) shows the electric field of the acceleration region with the measurement area as illustrated in Figure 4.5 (b). The axial measurement interval is 1.0 mm starting from 4.0 to 10.0 mm of the axial position from anode edge, and also the potential was measured at 3.5 mm of the axial position. In general, the potential contour near the channel exit is parallel to the channel exit plane up to around 3.0 mm from the channel center line on both sides. Ions will be accelerated along the center line in this area. The width of this area is almost to the distance between the exterior surfaces of anode (7.0 mm). On the contrary, the potential contour increases its radial component as the distance to the center axis increases, and the direction of the gradient of the potential reverses at a radial position of around 6.0 mm. Consequently, a portion of ions which exists in the outside area of anode will be accelerated toward the thruster causing erosion.

As a result, accelerating ions towards the center of the channel exit is important not only for the higher acceleration efficiency, but also for the reduction of erosion.

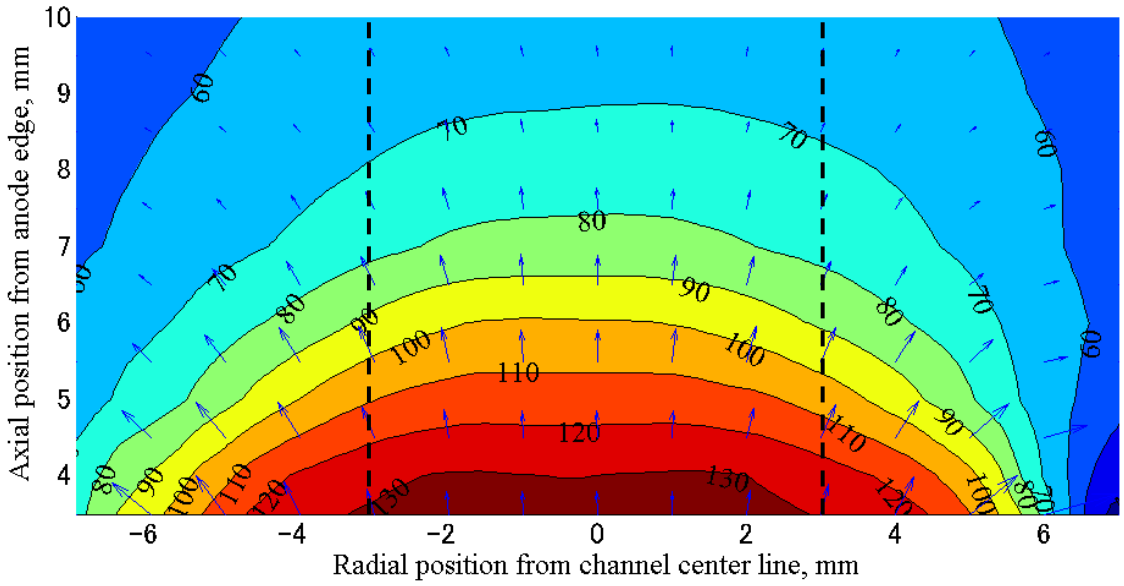

(a) Potential contour.

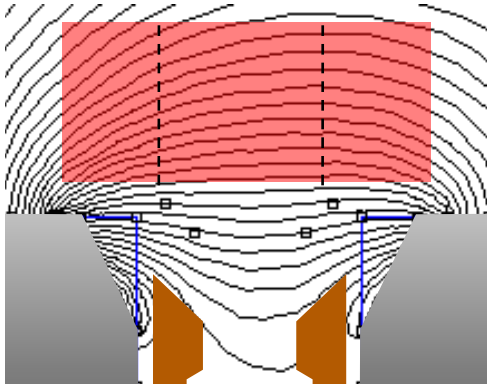

(b) Measured area (Red) and lines of magnetic force.

Figure 4.5 Electric field around acceleration region.

(V_d = 150 V, $\dot{m}$ = 1.95 mg/s, $|\boldsymbol{B}|$ = 55.6 mT)

4.4.2 Inside a Channel

The electric field inside the channel is shown in Figure 4.6 (a). The measurement was done at every 0.5 mm starting from 1.0 up to 3.0 mm of the axial position from the anode, and its width is 8.0 mm inside the channel and 10.0 mm outside. As described in Chapter 1.4, a steep potential gradient towards the wall had possibility to form inside the channel of TAL causing channel wall erosion by accelerating ions towards the wall. However, the potential gradient inside the channel is generally small, and there is no steep potential gradient towards the wall, which supports the contribution of the geometric configuration of magnetic shielding to the small channel wall erosion rate compared with a thruster without magnetic shielding as described in Chapter 4.1.

However, the potential contour inside the channel has a convex shape, accelerating partial ions toward the wall. Thus, for further restraint of the channel wall erosion, the potential contour has to be controlled to have a trough shape.

For the realization of the trough shape potential contour, modifications in the magnetic field configurations in addition to the geometric configuration would be necessary, as shown in Figure 4.7. Because the thruster configurations tested in this research was determined so that the magnetic flux density in a channel is sufficiently high, a slight difference exists in the magnetic field configurations between the ideal one and the design. Therefore, it can be expected that the modified thruster would have better performance in the channel wall erosion. Although the magnetic flux density of modified thruster shown in Figure 4.7 (b) is lower than the original shown in Figure 4.7 (a), the modified one would yield competitive performance compared with the original one with high magnetic flux density, because high power Hall thrusters, in general, require less magnetic flux density inside the channel.

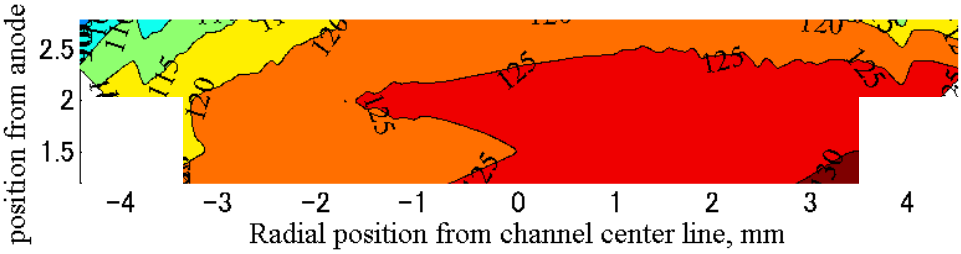

(a) Potential contour.

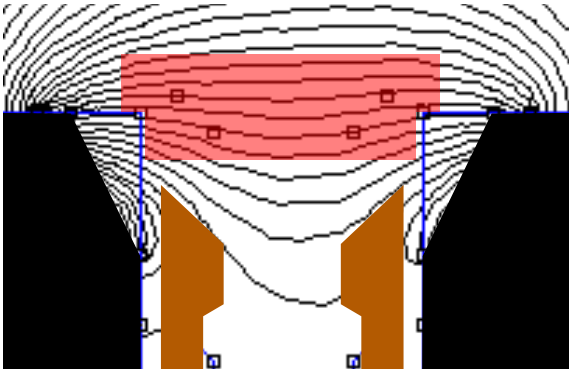

(b) Measured area (Red) and lines of magnetic force.

Figure 4.6 Electric field in a channel.

(V_d = 150 V, $\dot{m}$ = 1.95 mg/s, $|B|$ = 55.6 mT)

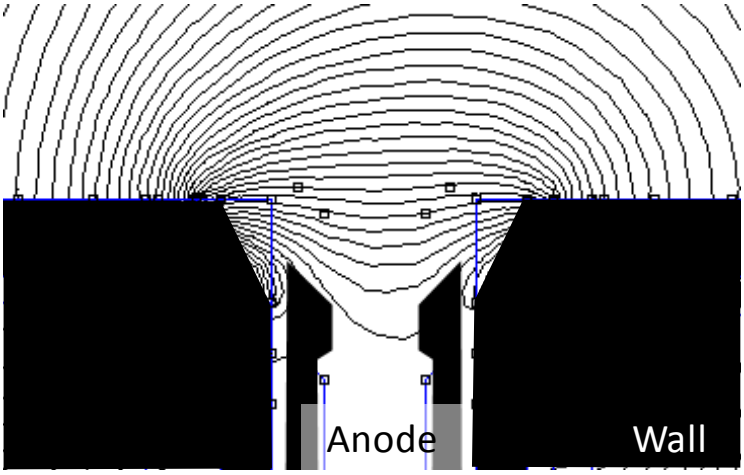

(a) A thruster configuration tested in this research.

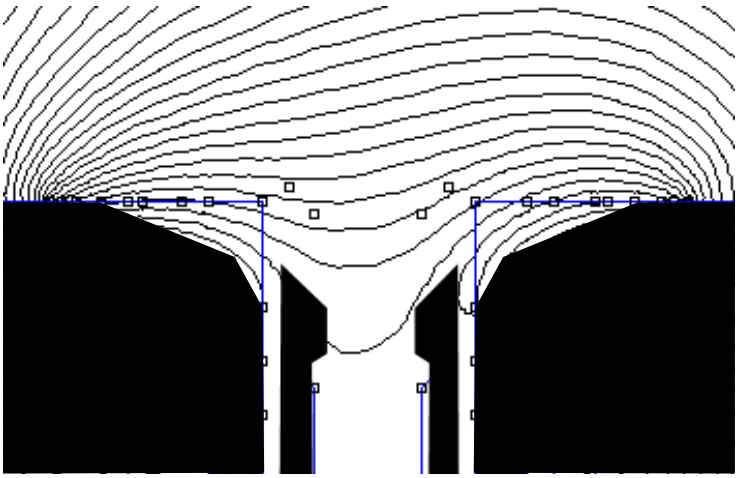

(b) A modified thruster configuration for zero-erosion.

Figure 4.7 Cross-section diagrams of the thruster tested in this research (Left) and modified thruster (Right).

4.5 Outlook of the Research

This study, so far, have measured an electric field in a channel enabling the prediction of trajectory of ions which have a given initial position. In addition, further evaluation of the channel wall erosion is possible by obtaining an ionization rate distribution to discuss the wall erosion rate quantitatively.

To obtain the ionization rate distribution, three physical quantity distributions are necessary: an electron number density, a neutral number density, and an electron temperature. The electron temperature has been already measured in this research. For the other two quantity distribution, a double probe measurement is the most suitable for the electron number density distribution assuming the plasma neutrality, and a numerical simulation is the best for the neutral number density distribution.

In summary, by measuring the electron number density distribution with a double probe and calculating the neutral number density distribution, the channel wall erosion can be evaluated quantitatively.

Chapter 5

Conclusion

For the realization of a zero-erosion Hall thruster, two investigation were conducted in this research: I) the derivation of the impact of zero-erosion Hall thruster on the feasibility of the construction of a SPS from the view point of a transportation cost, II) the measurement of an electric field in a channel of a TAL with a magnetic shield to examine the applicability of magnetic shielding to TAL, which has higher thrust efficiency than the conventional SPT, as well as to get the criteria for a zero-erosion Hall thruster.

The following knowledge was obtained from the two investigations.

I) The cost analysis of the construction of a 20,000 ton SPS using argon as propellant with optimized scenarios for the SPS construction:

1. Cost for propulsion system is 3.55 billion dollars, 64.9% of the total in-space transportation cost.
2. The lifetime of the thruster has a significant impact on the total in-space transportation cost: as the lifetime of the thruster increases twice as long, the cost decreases by 31%.

II) The investigation of a TAL with the geometric configuration of the magnetic shielding by evaluating the channel wall erosion rate, measuring electron temperature, and measuring an electric field in a channel:

1. Based on a measurement of a guard ring current, the channel wall erosion rate of UT-58 is lower than that of UT-38 without the geometric configuration of the magnetic shield.
2. From an axial electron temperature, the ionization region of UT-58 can be inferred to exist around the region 1 to 3 mm of the axial position from the anode edge.
3. The acceleration region starts from 0 up to 10 mm of the axial position from the anode edge. The potential difference between both ends of this acceleration region is 72.9 V, 48.6% of the discharge voltage.
4. In the acceleration region, the potential contour near the channel exit is parallel to the channel exit plane up to 6 mm of width, which is almost the width of anode exterior surface of 7 mm. On the contrary, the potential contour increases its radial components as the distance to the center axis increases.
5. A magnetic shield is applicable to TAL, judging from small potential gradient toward the wall.

For further investigation of the zero-erosion Hall thruster, the following studies are the most suitable.

1. Performance test of a thruster with modified configurations of magnetic field and geometry. This modification can have a negative influence on the thrust performance, thus, the study has to evaluate both the channel wall erosion performance and thrust performance.
2. The channel wall erosion can be evaluated quantitatively, by measuring the electron number density distribution with a double probe and calculating the neutral number density distribution.

Bibliography

[1] 栗木恭一 , 荒川義博, *電気推進ロケット入門*.: 東京大学出版会, 2003.

[2] Goebel, D. M. , Katz, I., *Fundamentals of Electric Propulsion: Ion and Hall Thrusters*.: Jet Propulsion Laboratory, California Institute of Technology, 2008.

[3] Nishiyama, K. , Kuninaka, H., "Discussion on Performance History and Operations of Hayabusa Ion Engines," *Transaction of JSASS, Aerospace Technology Japan*, vol. 10, no. ists28, pp. Tb_1-Tb_8, 2012.

[4] 小泉宏之, "第 32 回国際電気推進会議 (IEPC2011) 報告," *日本航空宇宙学会誌*, vol. 60, no. 5, pp. 203-205, May 2012.

[5] Kim, V. et al., "Electric Propulsion Activity in Russia," in *27th International Electric Propulsion Conference*, Pasadena, 2001, p. 05.

[6] Marchandise, F. et al., "PPS 1350-G Qualification Status 10500 h," in *30th International Electric Propulsion Conference*, Florence, 2007, p. 164.

[7] Koppel, C. R. , Estublier, D., "The SMART-1 Hall Effect Thruster Around the Moon: In Flight Experience," in *29th International Electric Propulsion Conference*, Princeton University, 2005, p. 119.

[8] Ozaki, T. et al., "Electric Propulsion Development Activity at MELCO," in *42nd AIAA/ASME/SAE/ASEE Joint Propulsion Conference & Exhibit*, Sacramento, 2006, p. 4321.

[9] Schönherr, T. et al., "Japan's Itinerary Towards High-Power Electric Propulsion," in *4th Russian-German Conference on Electric Propulsion*, Moscow, Dec. 2012, p. 60.

[10] Schönherr, T. et al., "Low-cost 20 kW Hall Thruster for Mass Transportation," in *Asian Joint Conference on Propulsion and Power*, Xi'an, Mar. 2012, p. 022.

[11] Schönherr, T. et al., "Design and Performance Evaluation of Thruster with Anode Layer UT-58 for High-Power Application," in *33rd International Electric Propulsion Conference*, Washington, D.C., 2013, p. 242.

[12] Arastu, A., "Advances in Technologies for High Power SEP Missions," in *10th International Energy Conversion Engineering Conference*, Atlanta, Aug. 2012.

[13] Soulas, G. C. et al., "Performance Test Results of the NASA-457M v2 Hall Thruster," in *48th AIAA/ASME/SAE/ASEE Joint Propulsion Conference & Exhibit*, Atlanta, 2012, p. 3940.

[14] Florenz, R. et al., "Electric Propulsion of a Different Class: The Challenges of Testing for Mega Watt Missions," in *48th AIAA/ASME/SAE/ASEE Joint Propulsion Conference & Exhibit*, Atlanta, 2012, p. 3942.

[15] V, S. A. et al., "Operating Envelopes of Thrusters with Anode Layer," in *27th International Electric Propulsion Conference*, Pasadena, 2001.

[16] Glaser, P., "Method and Apparatus for Converting Solar Radiation to Electric Power," A US3781647, Dec. 25, 1973.

[17] Sasaki, S. et al., "Tethered Solar Power Satellite," *JAXA Research and Development Report*, vol. JAXA RR-03-005E, pp. 1-12, 2004.

[18] Garner, C. E. et al., "Experimental Evaluation of Russian Anode Layer Thrusters," in *30th ASME/SAE/ASEE Joint Propulsion Conference & Exhibit*, Indianapolis, 1994, p. 3010.

[19] Nakles, M. R. et al., "A 205 Hour Krypton Propellant Life Test of the SPT-100 Operating at 2 kW," in *33rd International Electric Propulsion Conference*, Washington, D.C., 2013, p. 347.

[20] Grys, K. d. et al., "Demonstration of 10,4000 Hours of Operationi on a 4.5 kW Qualification Model Hall Thruster," in *46th AIAA/ASME/SAE/ASEE Joint Propulsion Conference & Exhibit*, Nashville, 2010, p. 6698.

[21] Hofer, R. R. et al., "Wear Test of a Magnetically Shielded Hall Thruster at 3000 Seconds Specific Impluse," in *33rd International Electric Propulsion Conference*, Washington, D.C., 2013, p. 033.

[22] Cho, S. et al., "Multilayer Coating Method for Investigating Channel Wall Erosion in a Hall Thruster," *Journal of Propulsion and Power*, vol. 29, no. 1, pp. 278-282, Jan. 2013.

[23] Huang, W. , Gallimore, A. D., "A Low-Cost Optical Approach to Evaluate the Life Time of Hall Thruster Discharge Channel," in *48th AIAA/ASME/SAE/ASEE Joint Propulsion Conference & Exhibit*, Atlanta, Aug. 2012, p. 4035.

[24] Cho, S. et al., "Channel Wall Erosion Modeling of a SPT-Type Hall Thruster," *Transaction of the Japan Society for Aeronautical and Space Sciences*, vol. 10, pp. Pb25-Pb30, 2012.

[25] Eagle, W. E. et al., "The Erosion Prediction Impact on Current Hall Thruster Model Development," in *44th AIAA/ASME/SAE/ASEE Joint Propulsion Conference & Exhibit*, Hartford, 2008, p. 5087.

[26] Yamamoto, N., Nakashima, H., Yalin, A. P., "Dependence of Lifetime on Magnetic Field Configuration in a Hall Thruster," in *48th AIAA/ASME/SAE/ASEE Joint Propulsion Conference & Exhibit*, Georgia, Aug. 2012, p. 3791.

[27] Mikellides, I. G. et al., "Magnetic Shielding of the Channel Walls in a Hall Plasma Accelerator," *Physics of Plasmas*, vol. 18, p. 03350, Mar. 2011.

[28] Mikellides, I. et al., "Design of a Laboratory Hall thruster with Magnetically Shielded Channel Walls, Phase III Comparison of Theory with Experiment," in *48th AIAA/ASME/SAE/ASEE Joint Propulsion Conference & Exhibit*, Atlanta, Aug. 2012, p. 3789.

[29] Chen, F. F., *Introduction to Plasma Physics and Controlled Fusion: Volume 1: Plasma Physics*, 2nd ed.: Plenum Publishing Corporation, 1983.

[30] プラズマ・核融合学会, *プラズマ診断の基礎と応用*.: コロナ社, 2006.

[31] Auciello, O. , Flamm, D. L., *Plasma Diagnostics: Discharge Parameters and Chemistry (Plasma Materials Interactions)*. San Diego, US: Academis Press, Inc., 1989.

[32] 山本学 , 村山精一, *プラズマの分光計測*.: 学会出版センター, 1995.

[33] 堤井信力, *プラズマ基礎工学*, 増補 ed.: 内田老鶴圃, 1995.

[34] Hargus, W. A., Jr., Cappelli, M. A., "Laser-Induced Fluorescence Measurements of Velocity within a Hall Discharge," *Applied Physics B*, vol. 72, pp. 961-969, May 2001.

[35] Yamamoto, N. et al., "Thomson Scattering Diagnostics in the Plasma of an Ion Thruster," *Transactions of the Japan Society for Aeronautical and Space Sciences*, vol. 10, pp. Pb79-Pb83, Jan. 2012.

[36] Huang, W., Gallimore, A. D., Smith, T. B., "Two-Axis Laser-Induced Fluorescence of Singly-Charged Xenon inside a 6-kW Hall Thruster," in *49th AIAA Aerospace Sciences Meeting including the New Horizons Forum and Aerospace Exposition*, Orlando, 2011, p. 1015.

[37] Dorval, N. et al., "Determination of the Ionization and Acceleration Zones in a Stationary Plasma Thruster by Optical Spectroscopy Study: Experiments and Model," *Journal of Applied Physics*, vol. 91, no. 8, pp. 4811-4817, Apr. 2002.

[38] Shastry, R. et al., "Plasma Potential and Langmuir Probe Measurements in the Near-field Plume of the NASA-457Mv2 Hall Thruster," in *48th AIAA/ASME/SAE/ASEE Joint Propulsion Conference & Exhibit*, Atlanta, 2012, p. 4196.

[39] Pétin, A. et al., "Time-Averaged and Time-Varying Plasma Potential in the Near-Field Plume of a Hall Thruster," in *33rd International Electric Propulsion Conference*, Washington, D.C., 2013, p. 214.

[40] Reid, B. M. , Gallimore, A. D., "Langmuir Probe Measurements in the Discharge Channel of a 6-kW Hall Thruster," in *44th AIAA/ASME/SAE/ASEE Joint Propulsion Conference & Exhibit*, Hartford, 2008, p. 4920.

[41] Smirnov, A., Raitses, Y., Fisch, N. J., "Plasma Measurements in a 100 W Cylindrical Hall Thruster," *Journal of Applied Physics*, vol. 95, no. 5, pp. 2283-2292, Mar. 2004.

[42] Staack, D., Raitses, Y., Fisch, N. J., "Shielded Electrostatic Probe for Nonperturbing Plasma Measurements in Hall Thrusters," *Review of Scientific Instruments*, vol. 75, no. 2, pp. 393-399, Feb. 2004.

[43] Reid, B. M. , Gallimore, A. D., "Plasma Potential Measurements in the Discharge Channel of a 6-kW Hall Thruster," in *44th AIAA/ASME/SAE/ASEE Joint Propulsion Conference & Exhibit*,

Hartford, 2008, p. 5185.

[44] Haas, J. M. et al., "Development of a High-Speed, Reciprocating Electrostatic Probe System for Hall Thruster Interrogation," *Review of Scientific Instruments*, vol. 71, no. 11, pp. 4131-4138, Nov. 2000.

[45] 雨宮宏 et al., "プローブ計測の基礎から応用まで," *Journal of Plasma and Fusion Research*, vol. 81, no. 7, pp. 482-523, July 2005.

[46] McDonald, M. S., Liang, R., Gallimore, A. D., "Practical Application of Wide Bandwidth Floating Emissive Probes and Wavelet Analysis to the X2 Nested Hall Thruster," in *33rd International Electric Propulsion Conference*, Washington, D.C., Oct. 2013, p. 352.

[47] Haas, J. M. , Gallimore, A. D., "Internal Plasma Potential Profiles in a Laboratory-Model Hall Thruster," *Physics of Plasmas*, vol. 8, no. 2, pp. 652-660, Feb. 2001.

[48] Knoll, A. et al., "Experimental Investigation of High Frequency Plasma Oscillation within Hall Thrusters," in *42nd AIAA/ASME/SAE/ASEE Joint Propulsion Conference & Exhibit*, Sacramento, 2006, p. 5171.

[49] Linnell, J. A. , Gallimore, A. D., "Internal Langmuir Probe Mapping of a Hall Thruster with Xenon and Krypton Propellant," in *42nd AIAA/ASME/SAE/ASEE Joint Propulsion Conference & Exhibit*, Sacramento, Jul. 2006, p. 4470.

[50] Godyak, V. A. , Demidov, V. I., "Probe Measurements of Electron-Energy Distributions in Plasmas: What Can We Measure and How Can We Achieve Reliable Results?," *Journal of Physics D*, vol. 44, p. 233001, May 2011.

[51] Gollor, M. et al., "Electric Propulsion Electronics Activities in Europe," in *47th AIAA/ASME/SAE/ASEE Joint Propulsion Conference & Exhibit*, San Diego, Aug. 2011, p. 5517.

[52] Brophy, R. et al., "300-kW Solar Electric Propulsion System Configuration for Human Exploration of Near-Earth Asteroids," in *47th AIAA/ASME/SAE/ASEE Joint Propulsion Conference & Exhibit*, San Diego, Aug. 2011, p. 5514.

[53] Sasaki, T., Imada, T., Takata, S., "Development Plan for Future Mission from HTV System," *Transaction of the Japan Society for Aeronautical and Space Sciences*, vol. 7, pp. Tk 77-82, 2010.

[54] Yelle, L., "The Learning Curve: Historical Review and Comprehensive Survey," *Decision Science*, vol. 10, no. 2, pp. 302-328, 1979.

[55] Alchian, A., "Reliability of Progress Curves in Airframe Production," *Econometrica*, vol. 31, no. 4, pp. 679-693, 1963.

[56] 荒川義博 et al., *イオンエンジンによる動力航行*: コロナ社, 2006.

[57] Hofer, R. , Randolph, T., "Mass and Cost Model for Selecting Thruster Size in Electric Propulsion Systems," in *47th AIAA/ASME/SAE/ASEE Joint Propulsion Conference & Exhibit*, San Diego, Aug. 2011, p. 5518.

[58] Bailey, S. et al., "The Future of Space Photovoltaics," in *Photovoltaic Specialists Conference*, Philadelphia, June 2009, pp. 001909-001913.

[59] Goebel, D. M., Crow, J. T., Forrester, A. T., "Lanthanum Hexaboride Hollow Cathode for Dense Plasma Production," *Review of Scientific Instruments*, vol. 49, pp. 469-472, 1978.

[60] Yamamoto, A. et al., "The Research on the Carbon Nano Tube Cathode," in *Particle Accelerator Conference*, Portland, 2003, pp. 3326-3328.

[61] 西山和孝 et al., "マイクロ波放電型中和器とホローカソードからの電磁雑音," *日本航空宇宙学会論文集*, vol. 49, pp. 84-91, 2001.

[62] Dote, T. , Amemiya, H., "Negative Characteristic of a Cylindrical Probe in a Magnetic Field," *Journal of the Physical Society of Japan*, vol. 19, no. 10, pp. 1915-1924, Oct. 1964.

[63] 細田誠也, "ホールスラスタ表面の絶縁体被膜によるイオン損失低減," 東京大学工学部航空宇宙工学科荒川・小紫研究室, 2010.

修士論文に関する発表一覧

(I) 国際会議 7 件 (筆頭著者 2 件, 共著 5 件)

1. **Ito, Y**, Nakano, M, Schönherr, T, Cho, S, Komurasaki, K and Koizumi, H, "In-Space Transportation of a Solar Power Satellite Using a Hall Thruster Propulsion System," in *International Conference on Renewable Energy Research and Applications*, Nagasaki, 2012, p.55.
2. **Ito, Y**, Nakano, M, Schönherr, T, Cho, S, Komurasaki, K, Koizumi, H, "Cost Evaluation of In-Space Transportation of a Solar Power Satellite Using OTVs with Hall thruster Propulsion Systems," in *29th International Symposium on Space Technology and Science*, Nagoya, 2013, p.o-1-05.
3. Schönherr, T, **Ito, Y**, Fujita, D, Kawashima, R, Koizumi, H, and, Komurasaki, K, "TAL Thruster Development for the Japanese High-Power In-Space Propulsion Project RAIJIN," *64st International Astronautical Congress*, Beijing, 2013, IAC-13-C4.4.2.
4. Schönherr, T, Fujita, D, **Ito, Y**, Kawashima, R, Cho, S, Koizumi, H, and, Komurasaki, K, "Argon anode-layer thruster for mass space transportation," *29th International Symposium on Space Technology and Science*, Nagoya, 2013, p.2013-o-1-03.
5. Schönherr, T, **Ito, Y**, Fujita, D, Kawashima, R, Koizumi, H, and, Komurasaki, K, "Influential parameters for discharge behavior and performance of anode-layer thruster," *31st International Conference on Phenomena in Ionized Gases*, Granada, 2013.
6. Schönherr, T, Kawashima, R, Koizumi, H, Komurasaki, K, Fujita, D, and **Ito, Y**, "Design and performance evaluation of thruster with anode layer UT-58 for high-power application," *33rd International Electric Propulsion Conference*, Washington, D.C., 2013, IEPC-2013-242.
7. Schönherr, T, Fujita, D, **Ito, Y**, Bambach, P, Suzuki, J, Kawashima, R, Koizumi, H, and, Komurasaki, K, "Performance evaluation and probe measurements of argon-based high-power thruster with anode layer UT-58," *Asian Joint Conference on Propulsion and Power 2014*, Nagoya, 2014.

(II) 国内会議 6 件 (筆頭著者 2 件, 共著 4 件)

1. **伊藤裕樹**, 小紫公也, Arnault, A, 福成雅史, 荒川義博, 小泉宏之, 中野正勝, "SPS 建設のための高比推力輸送システムの提案," in *第 15 回宇宙太陽発電システム(SPS) シンポジウム*, 仙台, 2012, p.19.
2. **伊藤裕樹**, バンバッハ・パトリック, 川嶋嶺, ショーンヘル・トニー, 小紫公也, 小泉宏之, "高速往復プローブによるホールスラスタ放電室内部プラズマ診断システ

ムの開発,” in *平成 25 年度宇宙輸送シンポジウム*, 神奈川, 2014, p.STEP-2013-052.

3. 中野正勝, **伊藤裕樹**, 小紫公也, “電気推進を用いた太陽発電衛星の輸送ミッション,” in *第 56 回宇宙科学技術連合講演会*, 大分, 2012, p.P05.
4. 張科寅, 川嶋嶺, 細田誠也, 藤田大樹, **伊藤裕樹**, 小紫公也, 小泉宏之, ショーンヘルトニー, 荒川義博, “250 mN 級ホールスラスタの数値寿命シミュレーション,” in *第 56 回宇宙科学技術連合講演会*, 大分, 2012, 2J06.
5. 藤田大樹, 川嶋嶺, **伊藤裕樹**, 赤木将平, 鈴木淳, Tony Schönherr, 小泉宏之, 小紫公也, “アルゴンアノードレイヤ型ホールスラスタの作動特性,” in *平成 25 年度宇宙輸送シンポジウム*, 神奈川, 2014, p.STEP-2013-054.
6. 鈴木淳, 藤田大樹, **伊藤裕樹**, Schönherr, Tony, 川嶋嶺, 赤木将平, 小紫公也, 小泉宏之, “アノードレイヤスラスタ UT-58 のアルゴン推進剤高電圧動作特性,” in *第 57 回宇宙科学技術連合講演会*, 鳥取, 2013, p.P05.